Title

Triose phosphate translocator drives carbohydrates/energetic shuttling from the chloroplast in *Chlamydomonas reinhardtii*

Weichao Huang[1]†*, Anagha Krishnan[2]†, Anastasija Plett[3], Michelle Meagher[4], Nicole Linka[3], Bijie Ren[1], Justin Findinier[1], Petra Redekop[1], Neda Fakhimi[1], Jin Xu[5], Rick G. Kim[1], Devin A. Karns[2], Nanette Boyle[4], Matthew C. Posewitz[2], Arthur R. Grossman[1]*

[1]Department of Plant Biology, Carnegie Institution for Science, Stanford, CA 94305, USA

[2]Department of Chemistry, Colorado School of Mines, Golden, CO 80401, USA

[3]Institute of Plant Biochemistry, Heinrich-Heine University Düsseldorf, 40225 Düsseldorf, Germany

[4]Department of Chemical and Biological Engineering, Colorado School of Mines, Golden, CO 80401, USA

[5]Department of Microbiology and Cell Science, Institute of Food and Agricultural Sciences (IFAS), University of Florida, Lake Alfred, 33885, FL, USA

†Authors contributed equally.

*Corresponding Author: Weichao Huang; Address: The Carnegie Institution for Science, 260 Panama St. Bldg. 100; Stanford, CA 94305; email: whuang@carnegiescience.edu

*Corresponding Author: Arthur R. Grossman; Address: The Carnegie Institution for Science, 260 Panama St. Bldg. 100; Stanford, CA 94305; email: agrossman@carnegiescience.edu

Abstract

Photosynthetic eukaryotic organisms contain several chloroplast-associated metabolite transporters that enable energetic/metabolic exchange between the chloroplast and other cellular compartments. In this study, we used the model photosynthetic alga *Chlamydomonas reinhardtii* to investigate a highly expressed chloroplast triose phosphate transporter. The chloroplast triose phosphate/phosphate translocator 3 (CreTPT3) showed high DHAP and 3-PGA transport activities in vitro using a yeast liposome uptake system. Null mutants for CreTPT3, generated by CRISPR-Cas9, resulted in a pleiotropic phenotype impacting photosynthetic activity, metabolite pools, carbon partitioning and storage, the redox status of the chloroplast, and the accumulation of reactive oxygen species. The results presented demonstrate that CreTPT3 is the major conduit on the chloroplast envelope for the intracellular distribution of fixed carbon and reductant. Its function is critical for optimizing the use of resources and supporting cell fitness, managing the chloroplast redox status and sustaining high rates of photosynthetic CO_2 fixation.

Introduction

Photosynthetic organisms have evolved numerous strategies to distribute fixed carbon among the different cellular compartments, maintaining a dynamic metabolic/redox balance that fuels growth and biosynthetic processes. However, the extent and characteristics of metabolite and reductant shuttling between the chloroplast and other cellular compartments have not been extensively analyzed despite its importance to cellular metabolism. The chloroplast is delineated by a double envelope membrane that contains several metabolite translocators that are part of the machinery that governs metabolic trafficking among the different cellular compartments(*1*, *2*). Various mechanisms have been proposed in the shuttling of fixed carbon and reducing equivalents between the chloroplast and cytoplasm. Studies with *Arabidopsis thaliana* revealed that the malate shuttle, which involves multiple malate dehydrogenases (MDH) and malate/OAA translocators (OMT), functions in the export of reductants from the chloroplast and also enables the cells to manage redox conditions in the chloroplast(*3*, *4*).

In addition to the malate shuttle, reduced carbon can be exported from the chloroplast by the triose phosphate (triose-P)/phosphate (Pi) translocator (TPT), which can also serve potentially as a means of exporting carbon from the chloroplast and a safety valve for eliminating excess reducing power from the chloroplast and lessening the potential for ROS accumulation and damage(*5*, *6*). The TPTs can potentially function as a major path for exchanging metabolites between the chloroplast and cytosol. Triose-Ps are generated during photosynthetic CO_2 fixation by Calvin-Benson-Bassham cycle (CBBC) activity that is supported by the reducing power/energy (NADPH/ATP) derived from photosynthetic electron transport. The TPTs reside on the inner chloroplast envelope membrane and can export triose-Ps, including glyceraldehyde 3-phosphate (G3P/GAP), dihydroxyacetone phosphate (DHAP), and 3-phosphoglycerate (3-PGA) across the chloroplast envelope membrane and into the cytosol in a 1:1 counter exchange for Pi(*5*–*7*). Various plants like tobacco and Arabidopsis, do not exhibit a strong phenotype if TPT is either eliminated or its level is reduced(*8*–*10*). A reduction in TPT activity can be compensated for by moving the assimilated carbon into a transitory starch pool that is subjected to accelerated turnover in the light(*8*, *9*, *11*), leading to the production of hexoses that can be exported from the chloroplast. Characterization of a double mutant (*tpt-1/adg1-1*) of Arabidopsis null for TPT (*tpt-1*) and starch synthesis (*adg1-1*) exhibited severely compromised photosynthetic capacity and growth(*10*, *12*).

While there are a few studies that demonstrate the functionalities of TPT proteins in single-celled photosynthetic organisms (red algae, apicomplexans, cryptophyte) based on the in vitro activity of these proteins in liposome transport assays(*13–15*), the impact of null mutations in genes encoding TPT proteins on the physiology of the cells has not been investigated so far. In this study, we used the unicellular green alga *Chlamydomonas reinhardtii* (Chlamydomonas throughout), a well-established model organism that has been extensively used to dissect various physiological processes, including photosynthesis and acclimation to environmental change. Chlamydomonas contains more than 30 TPT homologs; the informatic analyses of these proteins are still not refined enough to be certain of their substrate specificities and, in many cases, the transported metabolites are likely not a triose-P. Here we present work that approaches the questions: *i*) which of the TPTs is a triose-P/Pi translocator associated with the chloroplast envelope; *ii*) what are the roles of chloroplast TPTs in partitioning carbon and reductant in cells and sustaining central carbon metabolism; and finally, *iii*) do the TPTs contribute to dissipating excess reducing equivalents and balancing cellular redox conditions? Our study demonstrates, for the first time, the physiological impact of a null mutation of a highly expressed algal TPT gene.

We have focused this analysis on Chlamydomonas TPT3 (CreTPT3), which exhibits the strongest sequence similarity to plant chloroplast TPTs among the four predicted chloroplast associated CreTPTs, and is highly expressed over the diel cycle, especially during the light period. Through a series of in vitro and physiological analyses we demonstrate that CreTPT3 is essential for the exchange of fixed carbon, sustaining central carbon metabolism and maintaining intracellular redox balance.

Results

Features of the triose-P/Pi translocator (TPT) family

Candidate genes encoding triose-P/Pi transporters (TPT) in the Chlamydomonas genome were identified by blasting the Arabidopsis TPT protein to the Chlamydomonas genome. The TPT family is the largest drug/metabolite transporter (DMT) family in eukaryotes and includes triose-P and sugar-phosphate permeases that are associated with chloroplasts; many family members are still functionally uncharacterized(*16–18*). Chlamydomonas harbors ~32 genes encoding proteins of the TPT family, with four members (CreTPT1, 2, 3 and 25) predicted to have a transit peptide and be chloroplast-localized (**Supplementary Table 2**). To learn about the potential substrate

100 specificities of the four putative chloroplast CreTPTs, their amino acid sequences were aligned
101 with the plastidial phosphate transporters (PT) from Arabidopsis (AtPTs) (**Supplementary Fig.**
102 **2**).

103 Land plants harbor four classes of phosphate translocators on the inner plastid envelope, including
104 a glucose 6-phosphate transporter (GPT), a xylulose phosphate transporter (XPT), a
105 phosphoenolpyruvate transporter (PPT), and a triose-P translocator (TPT)(*6*, *19–22*). The ability
106 of the transporters to use triose-P/DHAP or 3-PGA is dependent on five highly conserved residues
107 (H184, K203, Y338, K359, and R360 in AtTPT1)(*13*, *22*). Only CreTPT3 and CreTPT25 contain
108 all five of these residues (H170, K189, Y322, K345, and R346 in CreTPT3) (**Supplementary Fig.**
109 **2**, **3**). In AtTPT1, residue F262 (F248 in Chlamydomonas) is thought to inhibit
110 phosphoenolpyruvate (PEP) access to the binding site; this residue is replaced by N in AtPPT1
111 (PPT)(*13*, *22*). CreTPT25 has M at position F248, indicating that unlike the other CreTPTs,
112 CreTPT25 might have higher preference for PEP (**Supplementary Fig. 3**). These findings suggest
113 that of the four chloroplast TPT family members, CreTPT3 is most likely to function in specifically
114 shuttling triose-P or 3-PGA across the chloroplast envelope.

115 Additionally, a phylogenic tree was constructed to help determine the specificities of the putative
116 CreTPTs. This tree includes all of the CreTPTs and the plastidial phosphate transporters (PT) from
117 *Arabidopsis thaliana* (AtPPT1, AtTPT1, AtGPT1 and AtXPT1). The CreTPT1, 2, 3 and 25 amino
118 acid sequences cluster with the different AtTPTs (**Fig. 1A**, **Supplementary Fig 3**), again
119 suggesting that these individual Chlamydomonas transporters have different substrate specificities.
120 Since CreTPT3 is most closely related to AtTPT1 (**Fig. 1A**, **Supplementary Fig. 3**), the major
121 triose-P permease in Arabidopsis, we considered CreTPT3 as the Chlamydomonas ortholog of
122 AtTPT1.

123 **TPT3 transport properties**

124 To help establish the physiological (in vivo) function of CreTPT3, its subcellular localization was
125 first experimentally confirmed in Chlamydomonas. The CreTPT3 coding sequence with its
126 putative chloroplast targeting sequence was fused with the VENUS tag (CreTPT3-VENUS) and
127 expressed under the control of its own promoter in the Chlamydomonas mutant null for CreTPT3.
128 As shown in **Fig. 1B**, CreTPT3-VENUS was localized to the chloroplast envelope.

129 To evaluate the substrate specificity of CreTPT3, it was heterologously expressed in
130 *Saccharomyces cerevisiae* (yeast) cells and the resulting recombinant protein was biochemically
131 analyzed using a liposome uptake system. The Cre*TPT3* gene was codon-optimized, expressed in
132 yeast (**Fig. 1C**), total cell membranes were isolated and then CreTPT3 was reconstituted into
133 liposomes(*15*, *23*). The chloroplast phosphate transporters in vascular plants can catalyze a strict
134 Pi/Pi homo-exchange in vitro. The reconstituted CreTPT3 in liposomes was able to catalyze the
135 signature Pi homo-exchange, whereas in the absence of a counter-exchange substrate, little Pi
136 uptake was detected. This result demonstrates that the recombinant CreTPT3 protein can function
137 in Pi/Pi homo-exchange in liposomes (**Fig. 1D**). In contrast, very low Pi uptake rates were observed
138 for liposomes reconstituted with membranes from yeast cells lacking CreTPT3 (**Supplementary**
139 **Fig. 4**), indicating that the detected Pi import activity was the result of CreTPT3 expression in
140 yeast.

141 To assess the substrate specificity, the initial rates of Pi uptake into liposomes preloaded with
142 saturating concentrations (30 mM) of various potential counter-exchange substrates were
143 determined. As **Fig. 1E** shows, CreTPT3 exhibited the highest activity when DHAP was used as
144 substrate. The relative initial velocity for Pi uptake in exchange for DHAP was slightly higher than
145 that of 3-PGA (3-PGA exhibited a 75% exchange rate relative to that of Pi/DHAP) while the Pi
146 uptake into liposomes preloaded with PEP was much less efficient (about 16% relative to the
147 Pi/DHAP exchange rate) (**Fig. 1E**). Pi import was negligible when CreTPT3 liposomes were
148 preloaded with Glc-6-P, Glc-1-P, Fru-6-P, and Gal-1-P (**Fig. 1E**).

149 Characterizations of the K_M and K_i of CreTPT3 were performed to determine the affinity of the
150 transporter for the various substrates. CreTPT3 has an apparent Michaelis-Menten constant (K_M)
151 value of 1.1 +/- 0.2 mM for Pi (**Fig. 1F**), which is comparable to the value obtained for the vascular
152 plant TPT ortholog(*6*). DHAP and 3-PGA competitively inhibited Pi uptake with an inhibition
153 constant (Ki) of 0.57 +/- 0.01 mM and 0.79 +/- 0.12 mM, respectively (**Fig. 1F**), suggesting that
154 CreTPT3 has a higher affinity for DHAP and 3-PGA than for Pi. In the case of PEP, no inhibition
155 of the Pi/Pi homo-exchange was observed, even at the non-physiologically high concentration of
156 5 mM. Overall, the results of this in vitro assay indicate that CreTPT3 has a typical plant-TPT
157 substrate spectrum (*6*). It can transport Pi, triose-P (DHAP) and 3-PGA in a counter-exchange
158 mode, however PEP might not be a physiologically relevant substrate for CreTPT3, as was shown

159 for apoplast TPT homologues in other organisms(*13*, *24*).

160 **Isolation of *tpt3* null mutants and their impact on cell growth**

161 To explore the role of CreTPT3 in trafficking carbon and reductant across the chloroplast envelope
162 in vivo, CRISPR knockouts of Cre*TPT3* were generated. We used the CRISPR-Cas9 editing
163 system to disrupt the Cre*TPT3* gene in exons 1 and 7, while at the same time integrating the
164 hygromycin marker gene (*AphVII*) into the edited site (**Supplementary Fig. 5A**). Multiple
165 independent knockouts of Cre*TPT3* were obtained, including *t3ko1*, with the marker gene inserted
166 into exon 1, and *t3ko2* and *t3ko3*, with the marker gene inserted into exon 7 (**Supplementary Fig.**
167 **5**, **6**) using specific sgRNA2 guides.

168 To elucidate the physiological roles of CreTPT3, we first examined growth of the parental WT
169 strain and the knockout mutants under either LL or ML. In contrast to WT cells, growth of the
170 Cre*TPT3* knockouts (*t3ko1*, *t3ko2*, *t3ko3*) was significantly reduced in LL on either
171 photoautotrophic (TP) or heterotrophic (TAP) agar medium (**Fig. 2A**, **Supplementary Fig. 7A**,
172 **D**), while the growth of the mutant in ML was completely blocked in both TP and TAP (**Fig. 2A**,
173 **Supplementary Fig. 7D**). Growth curves were also determined for WT and mutant cells in liquid
174 medium (TP) in both LL and ML (**Fig. 2B**, **C**); the results were in accord with those observed for
175 the agar medium growth assays. Additionally, *tpt3* mutant cells in both LL and ML exhibited an
176 increased cell diameter and formed clusters of cells that appear to be less able to separate following
177 division **(Supplementary Fig. 8A**, **B**). To further confirm that the growth phenotypes are a
178 consequence of the *tpt3* knockout, we introduced a wild-type copy of Cre*TPT3* fused to VENUS
179 into the mutant strains (**Supplementary Fig. 5B**). As demonstrated in **Fig. 2B-E**, ectopic
180 expression of the wild-type Cre*TPT3* in the *t3ko2* mutant (*C_T3KO2*) rescued the reduced growth
181 phenotype of the mutant in all light conditions tested in this study (LL/ML/HL).

182 We also analyzed the chlorophyll content of cells grown photoautotrophically upon transfer from
183 LL to ML (**Supplementary Fig. 1**) and found that *t3ko2* had reduced chlorophyll content relative
184 to WT cells after 24 h in ML (**Fig. 2D-F** and **Supplementary Fig. 9**). Cell numbers and total
185 chlorophyll were quantified following the LL to ML transition. The chlorophyll levels per cell
186 declined in all strains at 24 and 48 h following the transfer to ML; however, it was lower by more
187 than half in *t3ko2* (0.34 μg/10^6 cells) relative to either WT cells or the *C_T3KO2* rescued strain
188 (both ~0.72 μg/10^6 cells) after 24 h of ML (**Supplementary Fig. 9**), with some additional increase

189 for WT and *C_T3KO2* after 48 h of ML illumination (which might reflect some shading caused
190 by an increase in the cell density). Finally, when mutant cells were transferred to HL for 24 h they
191 became highly bleached (**Fig. 2E**).

192 Taken together, these results indicate that the activity of the CreTPT3 shuttle is essential for growth
193 over a range of light intensities (LL/ML/HL).

194 **The *tpt3* mutant exhibits hyper-accumulation of 'storage' carbon**

195 To explore the impact of the loss of CreTPT3 activity on carbon partitioning, we quantified carbon
196 storage (starch and lipids) following a transition of WT and the *t3ko2* mutant from LL to ML.
197 Lugol staining showed extensive starch accumulation in the *t3ko2* cells after a 48-h exposure to
198 ML, whereas WT cells were barely stained **(Fig. 3A)**. Furthermore, as shown in **Fig. 3B**, there is
199 an ~55-fold (WT and *t3ko2*: 13.29 and 0.24 µg starch/µg chlorophyll, respectively) increase in
200 starch accumulation (normalized to chlorophyll) in the *t3ko2* mutant after 24 h of illumination in
201 ML. The mutant also exhibited a ~24-fold increase in lipid accumulation (on a chlorophyll basis),
202 as monitored by Nile Red fluorescence, relative to WT and *C_T3KO2* over the same time period
203 (WT and *t3ko2*: 1038.93 and 41.98 Nile Red fluorescence/chlorophyll, respectively) (**Fig. 3C**, **D**).
204 Since the chlorophyll in the mutant was approximately 50% relative to that of WT cells after 24 h
205 in ML, the accumulated starch and lipid on a per cell basis would be ~25-fold for starch and ~12-
206 fold for lipid in the mutant relative to the WT strains. Furthermore, the mutant cells are much
207 bigger than WT cells (**Supplementary Fig. 8A**, **B**), which may reflect the large increase of storage
208 carbon that they accumulated. Accumulated starch granules in the stroma of ML-exposed *t3ko2*
209 cells are readily visualized under bright field light microscopy (**Supplementary Video 1A**, **B**).
210 These results suggest that the inability to transport triose-P between the chloroplast and the cytosol
211 through CreTPT3 resulted in a repartitioning of photosynthetic assimilates (carbon, reductant, and
212 ATP) toward the synthesis of both starch and neutral lipid.

213 **Cre*TPT3* deletion leads to accumulation of CBBC/glycolytic/gluconeogenic intermediates**

214 To understand the metabolic consequences of the loss of CreTPT3 on growth under LL and ML,
215 comparative metabolic analysis of WT and *t3ko2* mutant was performed on cells grown at LL and
216 after shifting them to ML for 45 min or 6 h. Pool sizes of various central carbon metabolites,
217 particularly those of the CBBC/glycolysis/gluconeogenesis pathways and intermediates of the

218 TCA/glyoxylate cycle (**Fig. 3F**), were quantified. Data was normalized to both chlorophyll content
219 (**Fig. 3E**) and cell number (**Supplementary Fig. 10B**). The fold-change in the quantity of each
220 metabolite in the mutant relative to WT under LL or at 45 min and 6 h after the switch to ML is
221 given in **Fig. 3G** and **Supplementary Fig. 10C**.

222 Under LL and following transfer to ML, the *t3ko2* mutant maintained a significantly larger pool
223 (2 to 6-fold) of glycolytic/gluconeogenic intermediates [DHAP, 3-PGA and FBP (all three shared
224 with CBBC), G6P, PEP], and of some metabolites of the CBBC pathway (E4P, RU5P/X5P, R5P)
225 compared to WT, suggesting that the loss of CreTPT3 results in a back-up of these metabolites
226 within the cell; our hypothesis is that they are accumulating inside the chloroplast due to the lack
227 of CreTPT3 activity. This is supported by the finding of marked accumulation of starch and TAG
228 in the mutant strain (**Fig. 3A-D**). While the pool sizes of fumarate and malate (metabolites of the
229 TCA/glyoxylate cycle) were similar in both strains under LL, following the transition of the cells
230 to ML, WT cells showed a significant increase in the pool sizes of those metabolites while the
231 mutant maintained a lower level, indicating that the loss of CreTPT3 either directly (by supplying
232 precursors) or indirectly (metabolic rewiring) impacts their levels.

233 Thus, the one primary function of CreTPT3 would be the export of photosynthetically-synthesized
234 reduced carbon, which would drive metabolic processes in the cytoplasm and other cellular
235 compartments, while importing Pi into the chloroplast to sustain ATP synthesis.

236 **The *tpt3* mutant has reduced PSII activity when grown in moderate light**

237 To understand the impact of the loss of CreTPT3 activity on photosynthetic electron transport
238 (PET), we quantified photosynthetic activities following a transition from LL to ML, as shown in
239 **Supplementary Fig. 1**. Photosynthetic O_2 evolution rates (OERs) were measured for WT, *t3ko2*
240 and *C_T3KO2* at a range of light intensities. LL acclimated WT, *t3ko2*, and *C_T3KO2* showed
241 comparable OER at intensities below 200 µmol photons m^{-2} s^{-1} while at saturating light intensities
242 of ≥600 µmol photons m^{-2} s^{-1}, the OER of *t3ko2* was diminished slightly relative to the WT and
243 complemented strain (**Fig. 4A**). Upon acclimation of the cells to ML for 24 h, the *t3ko2*
244 consistently displayed low OER relative to WT and *C_T3KO2* under all actinic light intensities
245 used (**Fig. 4B**).

246

247 The PSII quantum yield, ΦPSII, is maximum after a dark pre-incubation (Fv/Fm). The Fv/Fm in
248 the mutant grown in LL was similar to that of WT and *C_T3KO2* immediately following the dark
249 incubation (**Fig. 4C**). The LL-acclimated WT and *t3ko2* cells exhibited comparable ΦPSII values
250 when the actinic light intensity was below 100 µmol photons m^{-2} s^{-1}, but decreased by about 20-
251 25% when the actinic light was increased to 400 µmol photons m^{-2} s^{-1}; that decrease was
252 maintained even when the actinic light was raised to over 1,000 µmol photons m^{-2} s^{-1}
253 (**Supplementary Fig. 11**). In contrast, dark acclimated mutant cells that were exposed to ML for
254 6 h exhibited an Fv/Fm that was about 2-fold lower than that of WT and *C_T3KO2* and continued
255 to decline over a period of 24 h in ML, with a 3-fold decrease in Fv/Fm for *t3ko2* compared to that
256 of WT (**Fig. 4C**, **Supplementary Fig. 11**).

257 The oxidation of the PQ pool is the slowest step in the PET chain between PSII and PSI(*25*, *26*).
258 The redox potential of the PQ pool changes upon increasing the irradiance to which the cells are
259 exposed. Thus, the redox potential of the PQ pool serves as a biological measure for evaluating
260 the balance between the photochemistry of PSII and linear photosynthetic electron transport.
261 Changes of the redox state of the PQ pool (measured as 1-qL)(*27*) in LL and ML acclimated cells
262 were analyzed at increasing actinic light intensities (**Fig. 4D**, **Supplementary Fig. 12**). In LL-
263 grown cells, the PQ pool was significantly more reduced in *t3ko2* even at low level illumination
264 compared to that of WT and the rescued strain. When the actinic light intensity was elevated to
265 400 µmol photons m^{-2} s^{-1}, the reduction levels of the PQ pool increased for all strains, although it
266 was still much more reduced in *t3ko2* compared to that of WT and the rescued strains (**Fig. 4D**,
267 **Supplementary Fig. 12**).

268 For cells that had been acclimated to ML (6 h and 24 h), the PQ pool was already very highly
269 reduced in *t3ko2* following exposure to LL, while it remained highly oxidized for both the WT and
270 the rescued strain (**Fig. 4D**, **Supplementary Fig. 12**). The level of PQ reduction in ML-acclimated
271 *t3ko2* increased only slightly with an increase in the actinic light intensity (**Fig. 4D**,
272 **Supplementary Fig. 12**). There was also an increase in the PQ pool reduction of WT and
273 *C_T3KO2* as the light intensity was raised, however, even at the highest light intensity the WT and
274 rescued strains maintained a much more oxidized PQ pool than that of the mutant; the highest
275 levels of 1-qL for WT and *C_T3KO2* were still ~2-fold lower than that of *t3ko2* (**Fig. 4D**,
276 S**upplementary Fig. 12**). Overall, inactivation of CreTPT3 resulted in attenuated PSII activities

277 (Fv/Fm, OER) and hyper-reduction of the PQ pool, suggesting a block in electron flow
278 downstream of the PQ pool.

279 **Impact of *tpt3* mutant on PSI activity**

280 To determine if PSI activity was also impacted in the mutant cells, we analyzed PSI/P700
281 oxidation/reduction kinetics following exposure of LL-grown cells to ML. Levels of photo-
282 oxidizable P700 were similar in all LL-acclimated strains (**Fig. 4E**). However, after 6 h in ML, the
283 level of photo-oxidizable P700 declined in the mutant to ~40% of that in WT and *C_T3KO2* cells
284 (**Fig. 4F**), followed by slightly more inhibition of PSI activity after 24 h of exposure to ML (**Fig.**
285 **4G**). These deleterious impacts on photosynthetic electron transport likely reflect a defect in
286 routing carbon/energy out of the chloroplast, which in turn will cause hyper-accumulation of
287 reductant in the chloroplast, which would potentially result in a backup of PET, elevated ROS
288 accumulation and damage to the photosynthetic apparatus.

289 **CreTPT3 is crucial for balancing metabolite flux and chloroplast redox**

290 Photosynthetic organisms mainly accumulate ROS in chloroplasts and mitochondria as byproducts
291 of aerobic metabolism(*28*). To assay ROS production in the mutant, we used the fluorescent probe
292 CM-H2DCFDA which, upon exposure to increasing ROS levels, is converted to the green-
293 fluorescent molecule dichlorofluorescein (DCF). DCF fluorescence was visualized by confocal
294 microscopy. As shown in **Fig. 5A** and **B**, ROS levels in the *t3ko2* mutant were markedly increased
295 (~3-fold) after 48 h in ML, while no difference in the level was detected in WT cells.

296 For an alternative, dynamic method for evaluating redox changes in the chloroplast, we used the
297 redox sensitive green fluorescent protein roGFP2 (**Supplementary Fig. 13**) that was targeted to
298 the chloroplast stroma. Two cysteine residues were engineered into the roGFP2 to form a
299 reduction-oxidation-dependent disulfide bond that detects intracellular changes in ROS
300 accumulation(*29*). roGFP2 was shown to monitor ratiometric redox changes of glutathione(*29*, *30*).
301 The ascorbate–glutathione (GSH) system is central to ROS detoxification(*31*), with the redox
302 potential of glutathione reflecting ROS levels. LL-acclimated WT cells and the *t3ko2* mutant
303 exhibited similar levels of chloroplast roGFP oxidation (**Fig. 5C**). Upon transfer of WT cells to
304 ML, the oxidation level of roGFP in the chloroplast increased by ~2-fold after 1.5 h, compared to
305 that of WT cells maintained in LL, followed by a decrease after a 6 h ML exposure (**Fig. 5C**). The

306 changes of redox in WT upon a LL to ML transition is in accord with previous results(*32*, *33*).
307 Furthermore, the synthesis of both GSH and ascorbate increases when the redox balance is shifted
308 to a largely oxidized state after transferring cells to a higher light intensity, and recovers several
309 hours after the transfer(*32*, *33*) as the cells acclimate to the higher light conditions. A similar redox
310 pattern determined by chloroplast roGFP2 was observed for the *t3ko2* mutant after it was shifted
311 to ML, however, the mutant showed a much greater increase in chloroplast oxidative conditions,
312 with a 5.0-fold increase after 1.5 h, and a 2.0-fold increase after 6 h, or 1.8- and 1.6-fold higher
313 than the levels measured in WT cells (**Fig. 5C**).

314 As triose-P is exported to the cytosol by CreTPT3, it could potentially donate redox equivalents to
315 mitochondrial electron transport and alter mitochondrial ROS production. Therefore, we measured
316 mitochondrial redox levels at different light intensities in both WT and the *t3ko2* mutant using the
317 roGFP sensor targeted to the mitochondrion. Upon a LL to ML transition, neither WT nor *t3ko2*
318 displayed a change in fluorescence from the mitochondrial targeted roGFP (**Fig. 5D**). These results
319 suggest that the mitochondrial redox level is maintained after shifting either LL acclimated WT or
320 *t3ko2* cells to ML. This is in agreement with the results obtained for diatoms; the roGFP oxidation
321 level in diatom mitochondria exhibited either no or minor changes in response to various stress
322 conditions, including nitrogen limitation, HL, and iron limitation(*34*). Overall, these results
323 suggest that the increase in oxidative conditions caused by a LL to ML transition is primarily
324 localized to the chloroplast in Chlamydomonas and that the inability to export triose-P through
325 TPT3 markedly increases the chloroplast oxidative stress level.

326 Another issue that we addressed was whether CreTPT3 is important for dark metabolism in
327 Chlamydomonas. We analyzed redox changes in WT and the *t3ko2* mutant upon transferring cells
328 from LL to the dark. Intriguingly, ROS accumulation in WT was 5 times higher than that of *t3ko2*
329 after 48 h of darkness (**Fig. 5E**, **F**). The oxidation level of chloroplast roGFP2 in WT was slightly
330 reduced during the first 3 h of darkness, followed by a >1.5-fold increase after 6 h of darkness
331 compared to LL-acclimated cells (**Fig. 5G**). This is in keeping with previous observations in
332 Arabidopsis in which exposing leaves to extended darkness resulted in an initial decrease in the
333 degree of oxidation of roGFP2 in the chloroplast followed by an increase to the original LL level
334 when the darkness was prolonged(*35*). Unlike the slight decrease in roGFP2 oxidation in the WT
335 chloroplast, the oxidation state of the chloroplast in *t3ko2* cells declined by 2.2-fold relative to the

336 original LL conditions and by 1.77-fold relative to WT after 3 h in the dark (**Fig. 5G**). The
337 chloroplast oxidation level in *t3ko2* did not recover to the level of WT cells after 6 h of darkness
338 but attained its initial LL level after 24 h in the dark (**Fig. 5G**). The mitochondrial oxidation level
339 in *t3ko2* during the dark period was slightly but not strikingly higher than that in WT (**Fig. 5H**).
340 In sum, these results suggest that CreTPT3 also affects cellular redox levels in the dark.

341 In addition to the light conditions, we analyzed changes in the starch contents over the diel cycles.
342 As shown in **Fig. 5I**, *t3ko2* accumulates 7 times more starch than that of WT cells after 12 h in the
343 light (*t3ko2*, WT: 10.21, 1.403 µg starch/µg chlorophyll). Similar to WT and the rescued strain,
344 *t3ko2* can mobilize 70% of the starch at the end of the light period, indicating that *t3ko2* contains
345 much more carbohydrates in the chloroplast in the dark (**Fig. 5I**).

346 **Discussion**

347 Photoassimilates that serve as substrate for the chloroplast triose-P/Pi translocator (TPT) have been
348 studied in various vascular plants (e,g, tobacco, Arabidopsis, potato, etc). However, surprisingly
349 few studies have characterized chloroplast envelope localized members of the triose-P family in
350 trafficking fixed carbon in single-celled photosynthetic organisms(*13–15*); their physiological
351 role(s) in algae has not been elucidated. The Chlamydomonas genome encodes 4 putative triose-P
352 transporters predicted by TargetP-2.0 to be routed to the chloroplast. Cre*TPT3* is the most highly
353 expressed among the chloroplast associated TPTs (**Supplementary Table 3**, **Supplementary Fig.**
354 **14A**). A detailed analysis comparing Chlamydomonas TPT proteins with those of other organisms
355 revealed that CreTPT3 is most similar to the *Arabidopsis thaliana* TPT1 (**Fig. 1A**). In this study,
356 we localized CreTPT3 to the chloroplast envelope. To explore the function of CreTPT3, we
357 expressed it in yeast cells and performed in vitro studies to assay its activity in liposomes (**Fig.**
358 **1C-F**) and demonstrated the capacity of this translocator to use Pi, DHAP and 3-PGA as substrates
359 (**Fig. 1D-F**), similar to plant TPT(*6*). Hence, it appears that CreTPT3 can exchange
360 chloroplast/stromal triose-Ps for cytosolic Pi, and may also serve as redox shuttle by catalyzing
361 DHAP/3-PGA exchange. We also generated mutants disrupted for the Cre*TPT3* gene to examine
362 the impact of a loss of function mutant on the physiology of Chlamydomonas.

363 **CreTPT3 is critical for the distribution of photosynthate**

364 An Arabidopsis mutant for the chloroplast TPT was isolated 20 years ago(*10*). The growth and

365 photosynthesis of this mutant, designated *ape2*, was not affected under LL conditions(*9*), although
366 its starch content was slightly elevated relative to that of WT Arabidopsis(*9*). The absence of
367 AtTPT in LL-grown plants appeared to be fully compensated for by directing more photosynthate
368 toward starch synthesis and turning over the starch rapidly in the light to generate sugars like
369 hexose phosphate (hexose-P) and other metabolites that can be exported from the chloroplast.
370 Furthermore, while *ape2* grew in HL, its growth was attenuated relative to WT Arabidopsis(*9*),
371 although there was no detectable change in the level of starch(*10*). In potato, a 2-3-fold increase
372 in starch was observed in transgenic plants with diminished levels of the chloroplast targeted
373 TPT(*11*). The reduction in TPT activity led to a strong growth retardation during the young stages
374 of development. Similar to Arabidopsis, a tobacco strain with decreased TPT activity was able to
375 compensate for the defect by accelerating the synthesis and turnover of starch and the transport of
376 hexose from the chloroplast(*8*). These observations suggest that various vascular plants respond to
377 a defect in the export of triose-P from chloroplasts by moving the fixed carbon into a transient
378 starch pool that is converted to sucrose/glucose/glucose-P through accelerated hydrolysis.
379 Glucose-P and potentially other metabolites generated from starch degradation can then be
380 exported from the chloroplast and trafficked to sink organs, providing them with carbon skeletons
381 and energy for anabolic processes(*36*). In contrast, a deficiency of TPT in rice, which uses sucrose
382 stored in leaves as its major transitory form of fixed carbon rather than starch, led to reduced
383 photosynthetic rates and about a 2-fold decrease in the level of starch relative to WT plants(*37*).

384 To probe the in vivo function of CreTPT3, we generated multiple null mutants, designated *t3ko*
385 and characterized one of the mutants (*t3ko2)* and the rescued strain in depth. Our results show that
386 the flux of fixed carbon trafficked through the CreTPT3 is crucial for Chlamydomonas growth
387 under all light intensities tested, and that it becomes essential for survival at the higher intensities
388 (**Fig. 2**, **Supplementary Fig. 7**). Chlamydomonas, unlike plant cells, contains little intracellular
389 sucrose, with starch as its major form of storage carbon(*38*). In addition to a pronounced growth
390 phenotype, the *t3ko2* mutant exhibited a dramatic change in its carbon partitioning. After 24 h in
391 LL, *t3ko2* contained ~16-fold more starch than that of WT cells (**Supplementary Fig. 10A**). After
392 24 h in ML, the starch and lipid contents of *t3ko2* were 55 and 24-fold higher, respectively, than
393 that of WT cells (**Fig. 3A-D**).

394 Furthermore, in Arabidopsis, elimination of the chloroplast targeted TPT protein did not

395 significantly alter the profiles of metabolites of either the CBBC or the glycolytic/gluconeogenic
396 pathways, suggesting the occurrence of compensatory mechanisms that redirect carbon from the
397 chloroplast of the mutant plant(*39*). In contrast, a Chlamydomonas mutant null for Cre*TPT3*
398 exhibited a dramatic increase of most metabolites in the glycolytic/gluconeogenic pathways,
399 suggesting that triose-P exchange catalyzed by CreTPT3 was not readily compensated for by
400 alternative fixed carbon shuttles. CreTPT1, CreTPT2 and CreTPT25, the other shuttles that
401 potentially transport triose-P or hexose-P across the Chlamydomonas chloroplast envelope, are
402 unable to compensate (at RNA level) for the loss of CreTPT3 (**Supplementary Fig. 14B-D**). These
403 results demonstrate the critical role of CreTPT3 in shuttling photoassimilates in Chlamydomonas.
404 The retention/accumulation of photoassimilates in the chloroplast appears to redirect them toward
405 the synthesis of starch and lipid, which would cause a marked deficit of fixed carbon in other
406 cellular compartments, such as the cytoplasm and mitochondrion, and severely compromise
407 physiological processes including cell growth and division; a loss of CreTPT3 impacts carbon
408 partitioning and growth under all light conditions tested (LL/ML) **(Fig. 2**, **3**, **Supplementary Fig.**
409 **10**).

410 **Metabolic flux through CreTPT3 is essential for redox homeostasis**

411 Studies of photosynthetic activities of *t3ko2* in ML support our hypothesis that the mutant has a
412 reduced capacity to utilize metabolites for anabolic processes required for growth. The marked
413 alteration in metabolite pools observed in the mutant (**Fig. 3E**) could feedback on PET and
414 potentially elicits photosynthetic control, constricting electron flow at the cyt b_6f complex as a
415 consequence of the elevation of ΔpH across the thylakoid membranes(*40*, *41*). Such control would
416 result in hyper-reduction of the PQ pool (**Fig. 4D**) and reduced electron flow to PSI, which would
417 help protect PSI from photoinhibition. Furthermore, *t3ko2* cells are strongly photoinhibited
418 following their transfer from LL to ML, conditions that cause little change in PET of WT and
419 *C_T3KO2* (**Fig. 4B-C**). These results strongly suggest that CreTPT3 is essential for maintaining
420 the flow of fixed carbon and reductant from the chloroplast to the cytosol where it can be allocated
421 for various anabolic processes that support normal cell growth.

422 The malate-OAA shunt represents another route that, under high redox stress, might have
423 compensated for the loss of the CreTPT3 shuttle. Intriguingly, malate levels in *t3ko2* were 4-fold
424 lower than in WT cells following a transition from LL to ML (**Fig. 3E**, **G**) suggesting that the

425 malate-OAA shunt cannot compensate for a loss of CreTPT3 activity in Chlamydomonas. A
426 previous study of metabolic flux analysis during heterotrophic growth of Chlamydomonas showed
427 that the TPT shuttle is almost 10-fold more active than the malate-OAA shunt(*42*).

428 Cre*TPT3* is the most responsive/upregulated of the four Chlamydomonas, chloroplast localized
429 *TPT* genes following exposure of cells to nitrogen, sulfur or iron deprivation (**Supplementary Fig.**
430 **15 A-C**), which reinforces the hypothesis that it plays an important role in controlling chloroplast
431 redox conditions. Deprivation of Chlamydomonas for nitrogen or sulfur caused dramatic
432 attenuation of PET(*43*) as the cells elicited an array of 'energy management' strategies to balance
433 energy generation and utilization(*43*). Elevated NPQ, chlororespiration and lipid/starch
434 accumulation are well recognized mechanisms to dissipate excess light energy and minimize ROS
435 production in Chlamydomonas in response to nutrient deprivation(*43*). In this study, TPT3-
436 dependent chloroplast triose-P/Pi transport appears to be critical for exporting 'overflow'
437 electrons/reductant to other cellular compartments. When this function is compromised, the
438 chloroplast accumulates various metabolites, which results in altered substrate availability for
439 chloroplast-localized metabolic processes. Additionally, hyper-reduction of chloroplast redox
440 components, such as the PQ pool, and elevated production of ROS can lead to dysfunction of the
441 photosynthetic apparatus (and other metabolic activities), almost mirroring the response of the
442 cells to N-stress.

443 This study also suggests that CreTPT3 impacts the redox levels of the chloroplast in the dark. It
444 was proposed that during an extended period in the dark, Arabidopsis becomes sugar starved which
445 leads to the diminished availability of reductant for scavenging ROS(*35*, *44*). This hypothesis has
446 been supported by the transcriptome analysis of an Arabidopsis starch accumulation-defective
447 mutant (*pgm*) that has a lower sucrose level during the night than the WT plants(*45*). The
448 upregulation in the dark of the majority of the general ROS-induced transcripts in *pgm* is more
449 rapid than that of the WT, suggesting oxidative stress can be related to sugar starvation(*35*).
450 Although our interpretation is speculative, given the highly reducing state of the chloroplast and
451 the elevated accumulation of starch in the chloroplast in *t3ko2*, the mutant likely maintains elevated
452 levels of sugars in the chloroplast during the dark period as it mobilizes the high level of carbon
453 that was stored during the light period. Indeed, as shown in **Fig. 5I**, *t3ko2* accumulates a higher
454 amount of carbohydrates in the dark, potentially leading to a greater capacity to generate reduced

455 carbons that efficiently scavenge excess ROS in the dark.

456 **CreTPT3 is central to metabolic and redox networks**

457 ADP-glucose pyrophosphorylase (AGPase), a key enzyme in starch synthesis, is known to be
458 exquisitely sensitive to allosteric regulation; it is activated by 3-PGA and inhibited by Pi(*46*).
459 When the *t3ko2* mutant was exposed to LL, there was already a dramatic increase of 3-PGA (6-
460 fold) relative to WT cells (**Fig. 3E**, **G**). The loss of CreTPT3 might also lead to less import of Pi
461 into chloroplasts resulting in an elevated ratio of 3-PGA/Pi in *tpt3* compared to that of the WT
462 cells. Thus, even in LL, AGPase in the mutant would become active, which in turn would lead to
463 starch accumulation (**Supplementary Fig. 10A**).

464 In chloroplasts, the high reductant levels can also modulate the activity of various redox-sensitive
465 target proteins via thiol-based redox regulation. Chloroplasts harbor two thiol-based redox systems
466 that independently regulate plastid metabolism by communicating redox conditions to specific
467 target enzymes, thereby increasing or decreasing their activities. One system, FDX/TRX reductase,
468 obtains reducing equivalents from FDX (which is reduced by PET)(*47*), while the other involves
469 NADPH-TRX reductase (NTRC), which uses NADPH as its substrate(*48*). Both systems can
470 activate AGPase and starch biosynthesis(*49*, *50*). Elevated reduction of the PQ pool in *t3ko2*
471 compared to that of WT (**Fig. 4D**, **Supplementary Fig. 12**) could activate the FDX/TRX system
472 while increased NADPH availability in the mutant might be instrumental in activation of the
473 NTRC (NADPH-TRX reductase) system.

474 Additionally, the ROS levels in *t3ko2* (**Fig. 5A-C**) could potentially activate alternative regulatory
475 pathways. ROS was initially considered harmful, causing oxidative stress, damaging lipids,
476 proteins, and DNA, eventually resulting in cell death(*51*). Increasing evidence, however, suggests
477 that ROS can also function in diverse signaling pathways(*51*) that regulate various cellular
478 processes(*52*, *53*) such as growth, the cell cycle, senescence(*54*), and acclimation to stressful biotic
479 and abiotic conditions(*55*). ROS can also regulate expression of some chloroplast genes encoding
480 proteins associated with photosynthesis and modulation of PET(*56*). For example, ROS inhibits
481 *de novo* synthesis of the PSII reaction center protein D1, which would lead to photoinhibition
482 during high light acclimation(*57*, *58*). Moreover, when PSI becomes highly reduced, superoxide
483 and singlet oxygen both elicit PSI photoinhibition(*59*).

484 Overall, Chlamydomonas mutants lacking TPT3 develop a hyper-reduced chloroplast landscape
485 with elevated ROS production (**Fig. 5A-C**). After 6 h or more in ML, PSII and PSI activities in
486 the mutant become compromised, most likely a consequence of elevated ROS levels (see model
487 on **Fig. 6**). The chloroplast generated ROS serves as a messenger for reporting redox information
488 (e.g. light levels, stress conditions) to the regulatory machinery of the cell, which results in
489 modulation of expression of nuclear genes that would ameliorate the impact and damage associated
490 with elevated ROS levels(*60–62*). Many studies have shown that stress-induced
491 lipid/triacylglycerol (TAG) accumulation also correlates with an increase in ROS production(*63*);
492 ROS may activate diacylglycerol acyltransferases (DGAT) and phospholipid diacylglycerol
493 acyltransferase activities (PDAT) thereby stimulating lipid accumulation(*64*).

494 As depicted in **Fig. 6**, we propose that various tiers of redox regulation are potentially responsible
495 for the differential physiological responses of Chlamydomonas *tpt3* knockout mutants. When
496 *t3ko2* cells are initially transferred from LL to ML, the triose-P pool and metabolites derived from
497 that pool accumulate in the mutant because of its reduced capacity to move triose-P out of the
498 chloroplast, which also causes reduced CBBC activity, hyper-reduction of PET and the
499 accumulation of ROS (which would inhibit photosynthetic activity). The hyper-reduction of PET
500 and accumulation of carbon metabolites in the chloroplast of the *tpt3* mutants would activate
501 AGPase through allosteric regulation and by the FDX/TRX and NTRC redox systems, which
502 would result in starch hyper-accumulation (**Fig. 6**). Furthermore, increased ROS/RS accumulation
503 and the elevated redox state of PET would elicit retrograde signals that mediate changes in
504 expression of both chloroplast and nuclear genes, marshaling the synthesis of specific activities
505 that function to ameliorate the impact of the hyper-reduced state of the chloroplast resulting from
506 the compromised ability of the cells to export reductant and fixed carbon from the organelle (**Fig.**
507 **6**).

508 **Material and methods**

509 **Strains and culture conditions**

510 WT Chlamydomonas M10 (CC-4403, isogenic line derived from CC-124) was used as the parental
511 strain for the generation of knockout mutants. Cultures were routinely cultivated in growth
512 chambers (LED-41L2, Percival Scientific, Inc.) at 25°C with continuous shaking on an orbital

513 shaker (VWR OS-500 Shaker) at 120 rpm, in Tris-acetate-phosphate (TAP) medium(*65*). The
514 cultures were illuminated with continuous cool white LEDs at low light (LL, 30 µmol photons m^{-}
515 ^{2} s^{-1}). Experiments were mostly performed with cells grown in the photoautotrophic medium TP
516 (TAP medium without acetate), and in TAP medium in some cases, at 25ºC, and sparged with air
517 while being shaken at 120 rpm in a growth chamber (LED-41L2, Percival Scientific, Inc.). For
518 growth assays, cultures were inoculated at a density of 0.02 at $OD_{750\ nm}$ (~1×10^5 cells/mL) in TP
519 sparged with air under either LL or moderate light (ML, 250-300 µmol photons m^{-2} s^{-1}) intensities.

520 For spectrophotometric and chlorophyll fluorescence analyses, precultures were grown in TAP in
521 LL to mid-exponential phase, the cells were pelleted by centrifugation at 800xg, for 3 min at room
522 temperature, and the pellets were washed once with TP and then resuspended in TP at a density of
523 1-1.5 µg/mL chlorophyll. These cultures were grown in TP sparged with air and after 16-24 h in
524 LL, were transferred to ML. To avoid self-shading, the culture density was adjusted to 1-1.5 µg/mL
525 chlorophyll before ML exposure.

526 Cell samples exposed to the different light intensities were diluted to perform spot tests for
527 photoautotrophic growth on TP agar plates and for mixotrophic growth on TAP agar plates. Agar
528 plates were incubated for 7 d under either LL or ML (cool white LED) at 25°C.

529 **Phylogenetic analysis**

530 Protein sequences were aligned using MUSCLE(*66*). The best-fit nucleotide substitution model
531 was generated based on the Akaike information criterion (AIC) using MEGA7(*67*). Maximum
532 likelihood phylogenetic trees were constructed based on the best-fit model GTR (general time
533 reversible) + G (gamma distribution) + I (invariable sites) with 100 bootstrap replicates using
534 MEGA7(*67*).

535 **Expression of CreTPT3 in yeast**

536 The DNA sequence encoding the mature CreTPT3 protein was codon-optimized for expression in
537 *Saccharomyces cerevisiae* (GeneART, ThermoFisher Scientific). This coding sequence was
538 inserted in frame with an N-terminal His tag into the yeast vector pYES-NTa (ThermoFisher
539 Scientific) using Gibson cloning (NEB). Briefly, pYES-NTa was linearized with BamHI and the
540 CreTPT3 cDNA amplified with the primer pair fwd:5'-
541 gacgataaggtacctagcGCTTCTGCTGCTGATGCTC-3' and rev:5'-
542 agaattccaccacactgTTAAGCGGCAGCTGGAGAAG-3'. This cDNA was ligated into the

543 linearized pYES-NTa vector, which was then transformed into the yeast strain INVSc1 (MATa,
544 his3D1, leu2, trp1-289, ura3-52 / MATa, his3D1, leu2, trp1-289, and ura3-52, Thermo Fisher
545 Scientific) using the lithium-acetate/PEG method(*68*). Transformed yeast cells were selected on
546 synthetic complete medium containing 2% (w/v) glucose with the uracil auxotrophic marker.
547 Galactose-inducible expression of His-CreTPT3 in yeast was performed as described in(*15*). The
548 presence of the His-tagged fusion protein was verified by standard SDS-PAGE and immunoblot
549 analysis using an anti-His-antibody conjugated with horseradish peroxidase (Miltenyi Biotech).

550 **Reconstitution into liposomes and transport activity assays**

551 For uptake studies, yeast membranes from cells with and without recombinant His-CreTPT3 were
552 enriched and reconstituted into 3% (w/v) L-alpha-phosphatidylcholine using a freeze-thaw-
553 sonication procedure(*15*). The reconstituted liposomes were preloaded with 30 mM Pi or the
554 indicated phosphorylated metabolites that were tested as potential transport substrates. As a
555 negative control for antiport activity, liposomes were also generated without preloading. The
556 external counter-exchange substrate was removed via gel filtration on Sephadex G-25M columns
557 (GE Healthcare). Transport assays were initiated by adding 0.25 mM [alpha-^{32}P]-phosphoric acid
558 (6,000 Ci/mmol) and performed as previously described in Linka et al. (2008). The Km for Pi was
559 determined by measuring the initial velocity at each of six external Pi concentrations between 0.05
560 and 5 mM. To obtain competitive inhibition constants (Ki), the uptake of 0.25 mM Pi into
561 liposomes containing 30 mM Pi was measured over a 4 min period in the presence of increasing
562 external inhibitor concentrations (0.05 - 5 mM). Three biological replicates were performed for all
563 described experiments. GraphPad Prism software version 9.3.0 was used for non-linear regression
564 analyses of the kinetic data.

565 **Vector construction, transformation and complementation**

566 The pRam118_VENUS plasmid which harbors the VENUS gene and the *AphVII* cassette (confers
567 resistance to hygromycin) (Cre01.g045550)(*69*), was used to express Cre*TPT3* (Cre01.g045550).
568 This plasmid was linearized with HpaI (NEB). Primers: g*TPT3*_pRam118_f and
569 g*TPT3*_pRam118_r (**Supplementary Table 1**) were used to amplify Cre*TPT3* genomic DNA
570 containing an overlap with the linearized pRam118_VENUS vector. For generating the plasmid
571 pRam118-CreTPT3&VENUS, genomic DNA of Cre*TPT3* was assembled with
572 pRam118_VENUS plasmid using Gibson assembly(*70*). A 1,000 bp sequence upstream of

573 Cre*TPT3* and containing the promoter region of the gene was amplified using the primers
574 TPT3pro1000_f and TPT3pro1000_r (**Supplementary Table 1**). The 3' UTR of Cre*TPT3* was
575 amplified using TPT_3UTR_f and TPT3_3UTR_r (**Supplementary Table 1**). The *PSAD*
576 promoter and the *RBCS2* 3'UTR of pRam118-CreTPT3&VENUS were replaced by the amplified
577 fragments of the 1,000 bp upstream region and the 3' UTR of Cre*TPT3*, respectively. This final
578 vector, designated pRam118_CreTPT3, contains the original Cre*TPT3* promoter (driving
579 expression of Cre*TPT3*), the genomic DNA sequence of Cre*TPT3*, VENUS and the Cre*TPT3* 3'
580 UTR plus the *AphVII* cassette. The Chlamydomonas *tpt3* mutant was transformed by
581 electroporation with a total amount of 2 µg (~500 ng/µL) of pRam118_CreTPT3 that was
582 linearized with AseI. Next, the linearized plasmids were added into 250 µL of cell suspension at
583 the concentration of ~3×10^8 cells/mL per reaction. The GeneArt MAX Efficiency Transformation
584 Reagent for algae (Invitrogen) was used for introducing the plasmid by electroporation following
585 the instructions provided by the manufacturer. Transformants were selected on solid TAP medium
586 containing hygromycin (10 µg/mL; Enzo Life).

587 **Subcellular localization**

588 Drug resistant transformants were visualized for VENUS fluorescence as previously described(*69*).
589 In brief, transgenic cell lines resistant to hygromycin were screened for VENUS fluorescence using
590 a microplate reader (Infinite M1000; TECAN). Excitation and emission settings were as follows:
591 VENUS, excitation 515/12 nm and emission 550/12 nm; chlorophyll excitation 440/9 nm and
592 emission 680/20 nm. The TCS SP8 confocal laser-scanning microscope (Leica) was used to
593 visualize the VENUS fluorescence signal. Detailed methods for visualization can be found in(*69*).

594 **CRISPR-Cas9 mediated mutagenesis**

595 The protocol for disruption of Cre*TPT3* (Cre01.g045550) was adapted from(*71*). Chlamydomonas
596 WT strain CC-124 was used for mutant generation. WT cells were cultured under continuous light
597 (50 µmol photons m^{-2} s^{-1}) for 2 d to a density of 3-5×10^6 cells/mL. The cells were then concentrated
598 to 2×10^8 cells/mL in 0.5×TAP supplemented with 80 mM sucrose. Two single guide RNAs
599 (sgRNA) were designed by CHOPCHOP and synthesized by Integrated DNA Technologies (IDT).
600 The sequences of the generated sgRNA are: *TPT3*-sg1 (5′-
601 CGCUGGGCGTCACUUCCCGGCGG-3′) for editing of exon 1 and *TPT3*-sg2 (5′-
602 AAGGCCGCUAUCGCCAACGUGGG-3′) for editing of exon 7. Prior to electroporation, Cas9

603 (IDT) and sgRNAs were incubated together at 37 °C for 30 min. Approximately 500 ng PCR
604 product of the *AphVII* cassette, which confers resistance to hygromycin, was added to the RNP
605 (ribonucleoprotein) mixture. 250 µl aliquots were electroporated using Super Electroporator
606 NEPA21 type II (NEPA GENE). After 16 h of recovery in very low light (10-15 µmol photons m^{-}
607 ^{2} s^{-1}), cells were plated onto solid TAP medium containing 10 µg/mL hygromycin. Sense or
608 antisense-oriented knock-ins of *AphVII* were determined by amplification using primer pairs with
609 one primer annealing to the genomic sequence and the other to the inserted sequence
610 (**Supplementary Table 1**). The amplified fragments were sequenced to verify the insertion sites
611 (ELIM BIOPHARM, Hayward, USA).

612 **Complementation of mutants of Cre*TPT3***

613 Mutant strains were transformed with the linearized plasmid pRam118_CreTPT3 plasmid. After
614 transformation, transformants were selected in ML and then screened for VENUS fluorescence.
615 Colonies containing VENUS and an *AphVII* cassette knock-in at the Cas9 targeted site were
616 examined for accumulation of the CreTPT3 protein by immunoblots using CreTPT3 antibody
617 generated by GenScript USA Inc (Piscataway, USA). Colonies of immuno-positive cells were
618 subjected to growth complementation assays using spot tests under ML on solid TAP or TP
619 medium.

620 **P700 activity measurements**

621 Absorbance spectroscopy for P700 analyses was performed in dark adapted liquid cultures (15
622 µg/mL chlorophyll, in 20 mM HEPES-KOH, pH 7.2, and 10% ficoll) using a JTS-100
623 spectrophotometer (SpectroLogiX, TN). Actinic light was provided by an orange LED (165 µmol
624 photons m^{-2} s^{-1}) for PSI oxidation, followed by a saturating pulse and a dark incubation. 20 µM
625 DCMU and 1 mM hydroxylamine were added to the cell suspension to inhibit linear electron flow
626 (LEF) prior to the measurement. P_{700} activity was measured by monitoring the absorbance at 705
627 nm (interference filter 6 nm FWHM was used to create a narrow excitation beam); the absorbance
628 at 740 nm was used to correct for an unspecific contribution to the 705 nm signal(*72*).

629 **Chlorophyll fluorescence analysis**

630 Chlorophyll fluorescence, used to evaluate photosynthetic electron transport, was measured using
631 a DUAL PAM-100 fluorometer. Cells were acclimated in the dark for 20 min. Light curves were

632 generated by illuminating cells with increasing light intensities (0, 10, 50, 100, 200, 400, 800, 1000,
633 1200 μmol photons m^{-2} s^{-1}) for 2 min at each intensity. 1 mM CO_2 ($NaHCO_3$) was added to the
634 reaction mix as an electron receptor for the CBBC.

635 **ROS measurements and roGFP2 imaging analysis**

636 All strains were grown photoautotrophically under LL for 16-24 h. After dilution with fresh
637 medium, the cultures were transferred to ML or the dark for >48 h and then stained with CM-
638 H2DCFDA (Thermo Fisher Scientific) as described in(*73*) for detecting ROS. Briefly, after the
639 treatment (e.g. 48 h in ML), 10 million Chlamydomonas cells (treated in various ways) were
640 pelleted and washed once with 1×PBS. The cells were then resuspended in 1×PBS containing 8
641 μM CM-H2DCFDA and incubated at room temperature in the dark for 30 min. Following this
642 incubation, the cells were washed three times with 1×PBS buffer, the fluorescent signals were
643 either visualized using TCS SP8 confocal laser-scanning microscope (Leica) or quantified with a
644 microplate reader (Infinite M1000; TECAN). Excitation and emission settings for the microscope
645 were: 488 nm/510-530 nm HyD SMD hybrid detector for ROS, and 488 nm/650-700 nm-HyD
646 SMD hybrid detector for chlorophyll autofluorescence. Excitation and emission settings for the
647 plate reader were as follows: ROS excitation 488/5 nm and emission 530/12 nm; chlorophyll
648 excitation 514/5 nm and emission 690/5 nm.

649 Constructs containing chloroplast or mitochondria targeting sequences(*74*) fused to codon-
650 optimized roGFP2(*29*) were transformed into WT and mutant strains. Cells were cultured as shown
651 in **Supplementary Fig. 1**. Signals from the transformed lines were visualized using a TCS SP8
652 confocal laser-scanning microscope (Leica). Using the sequential setup of the SP8, roGFP2 signals
653 were collected at the emission wavelength of 510-550 nm immediately following excitation of
654 roGFP2 at 405 nm and 488 nm(*29*). The degree of roGFP2 oxidation was analyzed as the ratio of
655 the emission signals after excitation at 405 nm and 488 nm(*29*).

656 **Photosynthesis-Irradiance curve**

657 Photosynthesis-Irradiance curves were measured using a custom Pt-Ag/AgCl polarographic
658 electrode system (ALGI) with a water jacketed (for temperature-control), 1 mL glass reaction
659 chamber. The YSI 5331A electrodes (Yellow Springs Instruments) were polarized at −0.8 V. The
660 cultures used for the assays were concentrated to 2.5-5 μg mL^{-1} chlorophyll, supplemented with

661 15 µL of 0.5 M sodium bicarbonate in water and then purged with 1% CO_2/99% He. Using a gas
662 tight syringe, the sample was transferred into the reaction chamber that was also purged with 1%
663 CO_2/99% He. The rate of change in O_2 levels was measured sequentially at the light intensities
664 100, 200, 600, 1000 µmol photons m^{-2} s^{-1} (photosynthetic active radiation, PAR); each intensity
665 was maintained for 3-5 min followed by a 3-min intervening dark period, and then the light level
666 was raised to the next higher intensity (stepped change) until the full range of intensities was tested.
667 At 1,000 µmol photons m^{-2} s^{-1}, the light was held for 10 min followed by an 8-min dark period.
668 Before the measurement of each experimental series, the electrodes were calibrated with air (~21%
669 O_2) and 1% CO_2/99% He mixture (0% O_2). The initial slope of the response was used to determine
670 the O_2 evolution rate.

671 **Starch and TAG quantification**

672 Cells were grown under LL to mid-exponential phase. Cultures were then diluted to 0.5 µg/mL
673 chlorophyll with fresh medium and transferred to and then grown in ML for 24 h or more, as
674 indicated. Starch was measured using a modified method(*75*). In brief, cells were collected by
675 centrifugation and pigments extracted with methanol. Dried pellets were resuspended in water and
676 heated at 100°C to break the cells and release the starch. After cooling, amyloglucosidase and α-
677 amylase (2.25 U/mL) were used to hydrolyze the starch and the products of hydrolysis were
678 quantified using a Glucose Colorimetric Detection Kit (Thermo Fisher).

679 Intracellular triacylglycerol (TAG) levels were estimated by a fluorometric assay using the dye
680 Nile Red (Thermo Fisher)(*76*). A Nile Red solution (500 µg/mL in acetone) was added to 1 mL of
681 cell suspensions to a final concentration of 0.5 µg/mL. The samples were then incubated at room
682 temperature for 30 min, and the Nile Red fluorescence emission quantified at 575 nm after
683 excitation at 530 nm using a microplate reader (Infinite M1000; TECAN).

684 **Metabolic analysis**

685 Cells grown at LL were shifted to ML for 45 min or 6 h, as indicated. 45 mL of culture was rapidly
686 quenched in cold saline solution (-2 to -3°C), extracted using cold methanol and then analyzed by
687 LC-MS/MS. Quenching and analysis of metabolites were performed according to(*77*) with
688 modifications. The quenching solution, filtered saline (9 g/L NaCl), was prechilled to 4°C in a

689 refrigerator. 30 mL of the quenching solution was transferred to a 50 mL conical tube kept in an
690 ice bath mixed with salt to depress the temperature to between -3ºC and -1ºC. 15 mL of the culture
691 was rapidly plunged into the 30 mL of the quenching solution and the samples were centrifuged at
692 4,000 rpm for 10 min at 4ºC. Cell pellets were washed with fresh prechilled saline solution and
693 centrifuged again at 4,000 rpm for 10 min in a 2 mL centrifuge tube. For each replicate, 45 mL of
694 the culture was sampled and the cell pellets were pooled. Washed pellets were frozen at -80ºC
695 until extraction. Metabolite extraction and further analysis were modified from(*78*). A step-by-
696 step protocol is described in supplemental information (SI). All chemicals used for metabolite
697 extraction and LC-MS/MS analysis were Optima grade reagents.
698

References

1. F. Facchinelli, A. P. M. Weber, The metabolite transporters of the plastid envelope: an update. *Front. Plant Sci.* **2**, 50 (2011).

2. I. Haferkamp, S. Schmitz-Esser, The plant mitochondrial carrier family: functional and evolutionary aspects. *Front. Plant Sci.* **3**, 2 (2012).

3. Y. Zhao, H. Yu, J.-M. Zhou, S. M. Smith, J. Li, Malate Circulation: Linking Chloroplast Metabolism to Mitochondrial ROS. *Trends Plant Sci.* **25**, 446–454 (2020).

4. Y. Zhao, L. Luo, J. Xu, P. Xin, H. Guo, J. Wu, L. Bai, G. Wang, J. Chu, J. Zuo, H. Yu, X. Huang, J. Li, Malate transported from chloroplast to mitochondrion triggers production of ROS and PCD in *Arabidopsis thaliana*. *Cell Res.* **28**, 448–461 (2018).

5. R. Fliege, U.-I. Flügge, K. Werdan, H. W. Heldt, Specific transport of inorganic phosphate, 3-phosphoglycerate and triosephosphates across the inner membrane of the envelope in spinach chloroplasts. *Biochim. Biophys. Acta Bioenerg.* **502**, 232–247 (1978).

6. U. I. Flügge, K. Fischer, A. Gross, W. Sebald, F. Lottspeich, C. Eckerskorn, The triose phosphate-3-phosphoglycerate-phosphate translocator from spinach chloroplasts: nucleotide sequence of a full-length cDNA clone and import of the in vitro synthesized precursor protein into chloroplasts. *EMBO J.* **8**, 39–46 (1989).

7. Y. Lee, T. Nishizawa, M. Takemoto, K. Kumazaki, K. Yamashita, K. Hirata, A. Minoda, S. Nagatoishi, K. Tsumoto, R. Ishitani, O. Nureki, Crystal structure of the triose-phosphate/phosphate translocator in complex with inorganic phosphate (2017), , doi:10.2210/pdb5y78/pdb.

8. R. E. Häusler, N. H. Schlieben, B. Schulz, U. I. Flügge, Compensation of decreased triose phosphate/phosphate translocator activity by accelerated starch turnover and glucose transport in transgenic tobacco. *Planta*. **204**, 366–376 (1998).

9. R. G. Walters, D. G. Ibrahim, P. Horton, N. J. Kruger, A mutant of Arabidopsis lacking the triose-phosphate/phosphate translocator reveals metabolic regulation of starch breakdown in the light. *Plant Physiol.* **135**, 891–906 (2004).

10. A. Schneider, R. E. Häusler, Ü. Kolukisaoglu, R. Kunze, E. Van der Graaff, R. Schwacke, E. Catoni, M. Desimone, U. I. Flügge, An *Arabidopsis thaliana* knock-out mutant of the chloroplast triose phosphate/phosphate translocator is severely compromised only when starch synthesis, but not starch mobilisation is abolished. *Plant Journal* (2002), doi:10.1046/j.1365-313X.2002.01460.x.

11. J. W. Riesmeier, U. I. Flügge, B. Schulz, D. Heineke, H. W. Heldt, L. Willmitzer, W. B. Frommer, Antisense repression of the chloroplast triose phosphate translocator affects carbon partitioning in transgenic potato plants. *Proc. Natl. Acad. Sci. U. S. A.* **90**, 6160–6164 (1993).

734 12. L. Heinrichs, J. Schmitz, U.-I. Flügge, R. E. Häusler, The Mysterious Rescue of adg1-1/tpt-
735 2 - an Arabidopsis thaliana Double Mutant Impaired in Acclimation to High Light - by
736 Exogenously Supplied Sugars. *Front. Plant Sci.* **3**, 265 (2012).

737 13. D. Moog, A. Nozawa, Y. Tozawa, R. Kamikawa, Substrate specificity of plastid phosphate
738 transporters in a non-photosynthetic diatom and its implication in evolution of red alga-
739 derived complex plastids. *Sci. Rep.* **10**, 1167 (2020).

740 14. I. Haferkamp, P. Deschamps, M. Ast, W. Jeblick, U. Maier, S. Ball, H. E. Neuhaus, Molecular
741 and biochemical analysis of periplastidial starch metabolism in the cryptophyte *Guillardia*
742 *theta*. *Eukaryot. Cell*. **5**, 964–971 (2006).

743 15. M. Linka, A. Jamai, A. P. M. Weber, Functional characterization of the plastidic phosphate
744 translocator gene family from the thermo-acidophilic red alga *Galdieria sulphuraria* reveals
745 specific adaptations of primary carbon partitioning in green plants and red algae. *Plant*
746 *Physiol.* **148**, 1487–1496 (2008).

747 16. D. L. Jack, N. M. Yang, M. H. Saier Jr, The drug/metabolite transporter superfamily. *Eur. J.*
748 *Biochem.* **268**, 3620–3639 (2001).

749 17. S. Knappe, U.-I. Flügge, K. Fischer, Analysis of the plastidic phosphate translocator gene
750 family in Arabidopsis and identification of new phosphate translocator-homologous
751 transporters, classified by their putative substrate-binding site. *Plant Physiol.* **131**, 1178–1190
752 (2003).

753 18. A. P. M. Weber, M. Linka, D. Bhattacharya, Single, ancient origin of a plastid metabolite
754 translocator family in Plantae from an endomembrane-derived ancestor. *Eukaryot. Cell*. **5**,
755 609–612 (2006).

756 19. K. Fischer, B. Kammerer, M. Gutensohn, B. Arbinger, A. Weber, R. E. Hausler, U.-I. Flugge,
757 A new class of plastidic phosphate translocators: A putative link between primary and
758 secondary metabolism by the phosphoenolpyruvate/phosphate antiporter. *Plant Cell*. **9**, 453
759 (1997).

760 20. B. Kammerer, K. Fischer, B. Hilpert, S. Schubert, M. Gutensohn, A. Weber, U. I. Flügge,
761 Molecular characterization of a carbon transporter in plastids from heterotrophic tissues: the
762 glucose 6-phosphate/phosphate antiporter. *Plant Cell*. **10**, 105–117 (1998).

763 21. M. Eicks, V. Maurino, S. Knappe, U.-I. Flügge, K. Fischer, The plastidic pentose phosphate
764 translocator represents a link between the cytosolic and the plastidic pentose phosphate
765 pathways in plants. *Plant Physiol.* **128**, 512–522 (2002).

766 22. Y. Lee, T. Nishizawa, M. Takemoto, K. Kumazaki, K. Yamashita, K. Hirata, A. Minoda, S.
767 Nagatoishi, K. Tsumoto, R. Ishitani, O. Nureki, Structure of the triose-phosphate/phosphate
768 translocator reveals the basis of substrate specificity. *Nat Plants*. **3**, 825–832 (2017).

769 23. B. Loddenkötter, B. Kammerer, K. Fischer, U. I. Flügge, Expression of the functional mature
770 chloroplast triose phosphate translocator in yeast internal membranes and purification of the

771 histidine-tagged protein by a single metal-affinity chromatography step. *Proc. Natl. Acad. Sci.*
772 *U. S. A.* **90**, 2155–2159 (1993).

773 24. L. Lim, M. Linka, K. A. Mullin, A. P. M. Weber, G. I. McFadden, The carbon and energy
774 sources of the non-photosynthetic plastid in the malaria parasite. *FEBS Lett.* **584**, 549–554
775 (2010).

776 25. H. H. Stiehl, H. T. Witt, Quantitative Treatment of the Function of Plastoquinone in
777 Photosynthesis. *Zeitschrift für Naturforschung B*. **24**, 1588–1598 (1969).

778 26. J. M. Escoubas, M. Lomas, J. LaRoche, P. G. Falkowski, Light intensity regulation of cab
779 gene transcription is signaled by the redox state of the plastoquinone pool. *Proc. Natl. Acad.*
780 *Sci. U. S. A.* **92**, 10237–10241 (1995).

781 27. S. Saroussi, D. A. J. Karns, D. C. Thomas, C. Bloszies, O. Fiehn, M. C. Posewitz, A. R.
782 Grossman, Alternative outlets for sustaining photosynthetic electron transport during dark-
783 to-light transitions. *Proc. Natl. Acad. Sci. U. S. A.* **116**, 11518–11527 (2019).

784 28. B. Halliwell, Reactive species and antioxidants. Redox biology is a fundamental theme of
785 aerobic life. *Plant Physiol.* **141**, 312–322 (2006).

786 29. J. D. Vevea, D. M. Alessi Wolken, T. C. Swayne, A. B. White, L. A. Pon, Ratiometric
787 biosensors that measure mitochondrial redox state and ATP in living yeast cells. *J. Vis. Exp.*,
788 50633 (2013).

789 30. S. Dorion, J. C. Ouellet, J. Rivoal, Glutathione Metabolism in Plants under Stress: Beyond
790 Reactive Oxygen Species Detoxification. *Metabolites*. **11** (2021), p. 641.

791 31. C. H. Foyer, G. Noctor, Ascorbate and glutathione: the heart of the redox hub. *Plant Physiol.*
792 **155**, 2–18 (2011).

793 32. S.-T. Lin, C.-W. Chiou, Y.-L. Chu, Y. Hsiao, Y.-F. Tseng, Y.-C. Chen, H.-J. Chen, H.-Y.
794 Chang, T.-M. Lee, Enhanced Ascorbate Regeneration Via Dehydroascorbate Reductase
795 Confers Tolerance to Photo-Oxidative Stress in *Chlamydomonas reinhardtii*. *Plant Cell*
796 *Physiol.* **57**, 2104–2121 (2016).

797 33. A. Vidal-Meireles, J. Neupert, L. Zsigmond, L. Rosado-Souza, L. Kovács, V. Nagy, A.
798 Galambos, A. R. Fernie, R. Bock, S. Z. Tóth, Regulation of ascorbate biosynthesis in green
799 algae has evolved to enable rapid stress-induced response via the *VTC2* gene encoding GDP-
800 l-galactose phosphorylase. *New Phytol.* **214**, 668–681 (2017).

801 34. S. G. van Creveld, S. Rosenwasser, D. Schatz, I. Koren, A. Vardi, Early perturbation in
802 mitochondria redox homeostasis in response to environmental stress predicts cell fate in
803 diatoms. *ISME J.* **9**, 385–395 (2015).

804 35. S. Rosenwasser, I. Rot, E. Sollner, A. J. Meyer, Y. Smith, N. Leviatan, R. Fluhr, H. Friedman,
805 Organelles contribute differentially to reactive oxygen species-related events during extended
806 darkness. *Plant Physiol.* **156**, 185–201 (2011).

807 36. H. Winter, S. C. Huber, Regulation of sucrose metabolism in higher plants: localization and
808 regulation of activity of key enzymes. *Crit. Rev. Biochem. Mol. Biol.* **35**, 253–289 (2000).

809 37. S.-K. Lee, J.-S. Eom, L. M. Voll, C. M. Prasch, Y.-I. Park, T.-R. Hahn, S.-H. Ha, G. An, J.-
810 S. Jeon, Analysis of a triose phosphate/phosphate translocator-deficient mutant reveals a
811 limited capacity for starch synthesis in rice leaves. *Mol. Plant*. **7**, 1705–1708 (2014).

812 38. U. Klein, Intracellular Carbon Partitioning in *Chlamydomonas reinhardtii*. *Plant Physiol.* **85**,
813 892–897 (1987).

814 39. E. J. A. Hilgers, M. A. Schöttler, T. Mettler-Altmann, S. Krueger, P. Dörmann, M. Eicks, U.-
815 I. Flügge, R. E. Häusler, The Combined Loss of Triose Phosphate and Xylulose 5-
816 Phosphate/Phosphate Translocators Leads to Severe Growth Retardation and Impaired
817 Photosynthesis in *Arabidopsis thaliana* tpt/xpt Double Mutants. *Front. Plant Sci.* **9**, 1331
818 (2018).

819 40. P. Joliot, G. N. Johnson, Regulation of cyclic and linear electron flow in higher plants. *Proc.*
820 *Natl. Acad. Sci. U. S. A.* **108**, 13317–13322 (2011).

821 41. J. E. Johnson, J. A. Berry, The role of Cytochrome b_6f in the control of steady-state
822 photosynthesis: a conceptual and quantitative model. *Photosynth. Res.* **148**, 101–136 (2021).

823 42. N. R. Boyle, N. Sengupta, J. A. Morgan, Metabolic flux analysis of heterotrophic growth in
824 *Chlamydomonas reinhardtii*. *PLoS One*. **12**, e0177292 (2017).

825 43. S. Saroussi, E. Sanz-Luque, R. G. Kim, A. R. Grossman, Nutrient scavenging and energy
826 management: acclimation responses in nitrogen and sulfur deprived Chlamydomonas. *Curr.*
827 *Opin. Plant Biol.* **39**, 114–122 (2017).

828 44. B. Usadel, O. E. Bläsing, Y. Gibon, K. Retzlaff, M. Höhne, M. Günther, M. Stitt, Global
829 transcript levels respond to small changes of the carbon status during progressive exhaustion
830 of carbohydrates in *Arabidopsis rosettes*. *Plant Physiol.* **146**, 1834–1861 (2008).

831 45. O. E. Bläsing, Y. Gibon, M. Günther, M. Höhne, R. Morcuende, D. Osuna, O. Thimm, B.
832 Usadel, W.-R. Scheible, M. Stitt, Sugars and circadian regulation make major contributions
833 to the global regulation of diurnal gene expression in Arabidopsis. *Plant Cell*. **17**, 3257–3281
834 (2005).

835 46. J. Preiss, in *The Biochemistry of Plants* (Elsevier, 1988; http://dx.doi.org/10.1016/b978-0-08-
836 092615-5.50012-6), pp. 181–254.

837 47. Y. Meyer, W. Siala, T. Bashandy, C. Riondet, F. Vignols, J. P. Reichheld, Glutaredoxins and
838 thioredoxins in plants. *Biochim. Biophys. Acta*. **1783**, 589–600 (2008).

839 48. J. M. Pérez-Ruiz, F. J. Cejudo, A proposed reaction mechanism for rice NADPH thioredoxin
840 reductase C, an enzyme with protein disulfide reductase activity. *FEBS Lett.* **583**, 1399–1402
841 (2009).

842 49. M. A. Ballicora, J. B. Frueauf, Y. Fu, P. Schürmann, J. Preiss, Activation of the potato tuber
843 ADP-glucose pyrophosphorylase by thioredoxin. *J. Biol. Chem.* **275**, 1315–1320 (2000).

844 50. A. Lepistö, E. Pakula, J. Toivola, A. Krieger-Liszkay, F. Vignols, E. Rintamäki, Deletion of
845 chloroplast NADPH-dependent thioredoxin reductase results in inability to regulate starch
846 synthesis and causes stunted growth under short-day photoperiods. *J. Exp. Bot.* **64**, 3843–
847 3854 (2013).

848 51. M. Schieber, N. S. Chandel, ROS function in redox signaling and oxidative stress. *Curr. Biol.*
849 **24**, R453-62 (2014).

850 52. C. H. Foyer, G. Noctor, Redox Homeostasis and Antioxidant Signaling: A Metabolic
851 Interface between Stress Perception and Physiological Responses. *Plant Cell*. **17**, 1866–1875
852 (2005).

853 53. D. Wagner, D. Przybyla, R. op den Camp, C. Kim, F. Landgraf, K. P. Lee, M. Würsch, C.
854 Laloi, M. Nater, E. Hideg, K. Apel, The Genetic Basis of Singlet Oxygen–Induced Stress
855 Responses of *Arabidopsis thaliana*. *Science* (2004), doi:10.1126/science.1103178.

856 54. P. Zimmermann, U. Zentgraf, The correlation between oxidative stress and leaf senescence
857 during plant development. *Cell. Mol. Biol. Lett.* **10**, 515–534 (2005).

858 55. G. Miller, V. Shulaev, R. Mittler, Reactive oxygen signaling and abiotic stress. *Physiol. Plant.*
859 **133**, 481–489 (2008).

860 56. J. Yu, Y. Li, Z. Qin, S. Guo, Y. Li, Y. Miao, C. Song, S. Chen, S. Dai, Plant chloroplast stress
861 response: Insights from thiol redox proteomics. *Antioxid. Redox Signal.* **33**, 35–57 (2020).

862 57. Y. Nishiyama, H. Yamamoto, S. I. Allakhverdiev, M. Inaba, A. Yokota, N. Murata, Oxidative
863 stress inhibits the repair of photodamage to the photosynthetic machinery. *EMBO J.* **20**,
864 5587–5594 (2001).

865 58. K. Kojima, M. Oshita, Y. Nanjo, K. Kasai, Y. Tozawa, H. Hayashi, Y. Nishiyama, Oxidation
866 of elongation factor G inhibits the synthesis of the D1 protein of photosystem II. *Mol.*
867 *Microbiol.* **65**, 936–947 (2007).

868 59. D. Takagi, S. Takumi, M. Hashiguchi, T. Sejima, C. Miyake, Superoxide and singlet oxygen
869 produced within the thylakoid membranes both cause photosystem I photoinhibition. *Plant*
870 *Physiol.* **171**, 1626–1634 (2016).

871 60. M. Exposito-Rodriguez, P. P. Laissue, G. Yvon-Durocher, N. Smirnoff, P. M. Mullineaux,
872 Photosynthesis-dependent H_2O_2 transfer from chloroplasts to nuclei provides a high-light
873 signalling mechanism. *Nat. Commun.* **8** (2017), doi:10.1038/s41467-017-00074-w.

874 61. C. H. Foyer, Reactive oxygen species, oxidative signaling and the regulation of
875 photosynthesis. *Environ. Exp. Bot.* **154**, 134–142 (2018).

876 62. S. Wakao, K. K. Niyogi, Chlamydomonas as a model for reactive oxygen species signaling
877 and thiol redox regulation in the green lineage. *Plant Physiol.* **187**, 687–698 (2021).

878 63. K. Shi, Z. Gao, T.-Q. Shi, P. Song, L.-J. Ren, H. Huang, X.-J. Ji, Reactive oxygen species-
879 mediated cellular stress response and lipid accumulation in oleaginous microorganisms: The
880 state of the art and future perspectives. *Front. Microbiol.* **8**, 793 (2017).

881 64. N. Chouhan, E. Devadasu, R. M. Yadav, R. Subramanyam, Autophagy induced accumulation
882 of lipids in pgrl1 and pgr5 of *Chlamydomonas reinhardtii* under high light. *Front. Plant Sci.*
883 **12**, 752634 (2021).

884 65. E. H. Harris, *Chlamydomonas sourcebook: Introduction to Chlamydomonas and its*
885 *laboratory use* (Academic Press, ed. 2, 2009), *Chlamydomonas Sourcebook*.

886 66. R. C. Edgar, MUSCLE: multiple sequence alignment with high accuracy and high throughput.
887 *Nucleic Acids Res.* **32**, 1792–1797 (2004).

888 67. S. Kumar, G. Stecher, K. Tamura, MEGA7: Molecular Evolutionary Genetics Analysis
889 version 7.0 for bigger datasets. *Mol. Biol. Evol.* **33**, 1870–1874 (2016).

890 68. R. D. Gietz, R. H. Schiestl, High-efficiency yeast transformation using the LiAc/SS carrier
891 DNA/PEG method. *Nat. Protoc.* **2**, 31–34 (2007).

892 69. Y. Kaye, W. Huang, S. Clowez, S. Saroussi, A. Idoine, E. Sanz-Luque, A. R. Grossman, The
893 mitochondrial alternative oxidase from *Chlamydomonas reinhardtii* enables survival in high
894 light. *J. Biol. Chem.* **294**, 1380–1395 (2019).

895 70. D. G. Gibson, L. Young, R.-Y. Chuang, J. C. Venter, C. A. Hutchison 3rd, H. O. Smith,
896 Enzymatic assembly of DNA molecules up to several hundred kilobases. *Nat. Methods*. **6**,
897 343–345 (2009).

898 71. J. Findinier, C. Delevoye, M. M. Cohen, The dynamin-like protein Fzl promotes thylakoid
899 fusion and resistance to light stress in *Chlamydomonas reinhardtii*. *PLoS Genet.* **15**,
900 e1008047 (2019).

901 72. S. Clowez, C. Renicke, J. R. Pringle, A. R. Grossman, Impact of Menthol on Growth and
902 Photosynthetic Function of *Breviolum Minutum* (Dinoflagellata, Dinophyceae,
903 Symbiodiniaceae) and Interactions with its Aiptasia Host. *J. Phycol.* **57**, 245–257 (2021).

904 73. F. Kong, A. Burlacot, Y. Liang, B. Légeret, S. Alseekh, Y. Brotman, A. R. Fernie, A. Krieger-
905 Liszkay, F. Beisson, G. Peltier, Y. Li-Beisson, Interorganelle Communication: Peroxisomal
906 MALATE DEHYDROGENASE2 Connects Lipid Catabolism to Photosynthesis through
907 Redox Coupling in Chlamydomonas. *Plant Cell*. **30**, 1824–1847 (2018).

908 74. P. Crozet, F. J. Navarro, F. Willmund, P. Mehrshahi, K. Bakowski, K. J. Lauersen, M.-E.
909 Pérez-Pérez, P. Auroy, A. Gorchs Rovira, S. Sauret-Gueto, J. Niemeyer, B. Spaniol, J. Theis,
910 R. Trösch, L.-D. Westrich, K. Vavitsas, T. Baier, W. Hübner, F. de Carpentier, M. Cassarini,
911 A. Danon, J. Henri, C. H. Marchand, M. de Mia, K. Sarkissian, D. C. Baulcombe, G. Peltier,

912 J.-L. Crespo, O. Kruse, P.-E. Jensen, M. Schroda, A. G. Smith, S. D. Lemaire, Birth of a
913 Photosynthetic Chassis: A MoClo Toolkit Enabling Synthetic Biology in the Microalga
914 *Chlamydomonas reinhardtii*. *ACS Synth. Biol.* **7**, 2074–2086 (2018).

915 75. U. Klein, A. Betz, Fermentative metabolism of hydrogen-evolving *Chlamydomonas*
916 *moewusii*. *Plant Physiol.* **61**, 953–956 (1978).

917 76. E. T. Yu, F. J. Zendejas, P. D. Lane, S. Gaucher, B. A. Simmons, T. W. Lane, Triacylglycerol
918 accumulation and profiling in the model diatoms *Thalassiosira pseudonana* and
919 *Phaeodactylum tricornutum* (Baccilariophyceae) during starvation. *J. Appl. Phycol.* **21**, 669–
920 681 (2009).

921 77. C. L. Sake, D. M. Newman, N. R. Boyle, Evaluation of quenching methods for metabolite
922 recovery in photoautotrophic *Synechococcus sp*. PCC 7002. *Biotechnol. Prog.* **36**, e3015
923 (2020).

924 78. J. D. Young, A. A. Shastri, G. Stephanopoulos, J. A. Morgan, Mapping photoautotrophic
925 metabolism with isotopically nonstationary (13)C flux analysis. *Metab. Eng.* **13**, 656–665
926 (2011).

927 79. X. Johnson, J. Alric, Central carbon metabolism and electron transport in *Chlamydomonas*
928 *reinhardtii*: metabolic constraints for carbon partitioning between oil and starch. *Eukaryot.*
929 *Cell*. **12**, 776–793 (2013).

930 80. C. L. Winder, W. B. Dunn, S. Schuler, D. Broadhurst, R. Jarvis, G. M. Stephens, R. Goodacre,
931 Global metabolic profiling of *Escherichia coli* cultures: an evaluation of methods for
932 quenching and extraction of intracellular metabolites. *Anal. Chem.* **80**, 2939–2948 (2008).

933 81. D. Strenkert, S. Schmollinger, S. D. Gallaher, P. A. Salomé, S. O. Purvine, C. D. Nicora, T.
934 Mettler-Altmann, E. Soubeyrand, A. P. M. Weber, M. S. Lipton, G. J. Basset, S. S. Merchant,
935 Multiomics resolution of molecular events during a day in the life of Chlamydomonas. *Proc.*
936 *Natl. Acad. Sci. U. S. A.* **116**, 2374–2383 (2019).

937 82. J. M. Zones, I. K. Blaby, S. S. Merchant, J. G. Umen, High-Resolution Profiling of a
938 Synchronized Diurnal Transcriptome from *Chlamydomonas reinhardtii* Reveals Continuous
939 Cell and Metabolic Differentiation. *Plant Cell*. **27**, 2743–2769 (2015).

940 83. C. Y. Ngan, C.-H. Wong, C. Choi, Y. Yoshinaga, K. Louie, J. Jia, C. Chen, B. Bowen, H.
941 Cheng, L. Leonelli, R. Kuo, R. Baran, J. G. García-Cerdán, A. Pratap, M. Wang, J. Lim, H.
942 Tice, C. Daum, J. Xu, T. Northen, A. Visel, J. Bristow, K. K. Niyogi, C.-L. Wei, Lineage-
943 specific chromatin signatures reveal a regulator of lipid metabolism in microalgae. *Nat Plants*.
944 **1**, 15107 (2015).

945 84. D. González-Ballester, D. Casero, S. Cokus, M. Pellegrini, S. S. Merchant, A. R. Grossman,
946 RNA-seq analysis of sulfur-deprived Chlamydomonas cells reveals aspects of acclimation
947 critical for cell survival. *Plant Cell*. **22**, 2058–2084 (2010).

85. E. I. Urzica, A. Vieler, A. Hong-Hermesdorf, M. D. Page, D. Casero, S. D. Gallaher, J. Kropat, M. Pellegrini, C. Benning, S. S. Merchant, Remodeling of membrane lipids in iron-starved Chlamydomonas. *J. Biol. Chem.* **288**, 30246–30258 (2013).

Acknowledgments:

WH thanks M. Onishi for advice on generation of CRISPR mutants and A. Burlacot for help with PQ pool measurements. WH also would like to thank N. Linka, N. Boyle, A. Plett, and M. Meagher for the contributions to the in vitro test and metabolomic analyses.

Funding:

This project has received funding from DOE award DE-SC0019417. WH was supported solely by a grant from the US Department of Energy, Office of Science, Basic Energy Systems (DE-SC0019417). AK and MCP were supported solely by a grant from the US Department of Energy, Office of Science, Basic Energy Systems (DE-SC0019341). NB and MM were supported by US Department of Energy, Office of Science, Office of Biological and Environmental Research (BER), (DE-SC0018301). NL and AP were supported by German Research Foundations (DFG Grant LI1781/2-2). BR was supported by National Science Foundation (Award Number: 1645164). RGK and JF were supported by the Department of Plant Biology of the Carnegie Institution for Science. PR was supported by Human Frontier Science Program (HFSP) RGP0046/2018 (to ARG).

Author contributions:

WH, AK, ARG and MP conceptualized the study. WH generated the CRISPR mutants as well as the complemented strain, localized the TPT3 protein, analyzed the redox status in the cell, performed respiration measurements, measured the reduction level of PQ pool, analyzed changes of starch over the diel cycle. AK performed the experiments of photosynthetic O_2 evolution, extraction of samples for LC-MS/MS, data analysis of LC-MS/MS. AP and NL performed the reconstitution into liposomes and transport activity assays. MM and NB performed LC-MS/MS and analyses of metabolite data. BR performed data mining for transcriptome and the Nile red staining. JF and NF analyzed starch changes upon transition from LL to ML. WH, PR and ARG analyzed PSI and PSII activities. JF and BR constructed roGFP2 associated vectors. JX and WH performed the phylogenetic tree. WH drafted the manuscript. ARG, MP, AK, NL, NB, AP, MM and all the other authors helped with revising and finalizing the manuscript.

Competing interests:

All other authors declare they have no competing interests.

Data and materials availability:

All data are available in the main text or the supplementary materials.

985 **Figures and Tables**

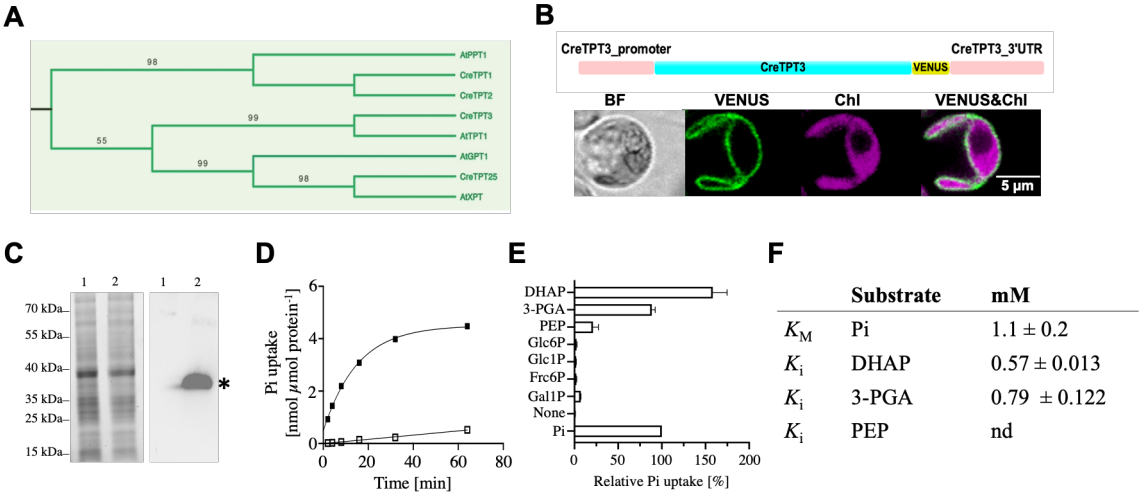

	Substrate	mM
K_M	Pi	1.1 ± 0.2
K_i	DHAP	0.57 ± 0.013
K_i	3-PGA	0.79 ± 0.122
K_i	PEP	nd

986

987 **Fig. 1: Chloroplast TPT phylogenies, subcellular localization of CreTPT3 and in vitro**
988 **measurements of CreTPT3 transport activities.** (**A**) Truncated phylogenetic tree of potential
989 chloroplast CreTPTs. (**B**) Cellular localization of CreTPT3. The construct for expression of the
990 CreTPT3-VENUS fusion protein is shown above the cell images and described in the Materials
991 and Methods. VENUS fluorescence, green; Chlorophyll (Chl) autofluorescence, magenta. (Scale
992 bar: 5 µm). (**C**) Expression of Cre*TPT3* in yeast. Left, SDS-PAGE gel of proteins from total
993 membranes isolated from yeast cells containing the empty vector (lane 1) or expressing His-
994 CreTPT3 (lane 2). Right, corresponding immunoblot blot detection of recombinant His-CreTPT3
995 protein using anti-His antibodies. The calculated molecular mass of the N-terminal His-tagged
996 protein was 37 kDa. (**D**) The kinetics of Pi exchange by His-CreTPT3 in lipid vesicles. Uptake of
997 Pi (0.25 mM) into liposomes was measured in the presence (■) or absence (□) of Pi (30 mM)
998 loaded within the vesicles. The arithmetic mean (±SD) of three independent experiments (each
999 consisting of three technical replicates) was plotted with respect to the time after initiating the
1000 assay. (**E**) Analyses of substrate specificity of His-CreTPT3. Liposomes in which His-CreTPT3
1001 was incorporated were preloaded with various substrates (30 mM) and the initial Pi uptake rates
1002 (at 0.25 mM external concentration) were determined. Relative velocities were compared to the
1003 Pi/Pi homo-exchange, which was set to 100%. The data represents the arithmetic mean (±SD) of
1004 three independent experiments (each consisting of three technical replicates). (**F**) Comparison of
1005 kinetic constants of CreTPT3. The Michaelis-Menten constant (K_M) for Pi uptake was determined
1006 using various external Pi concentrations (0.05-5 mM). The competitive inhibition constant (K_i) of
1007 Pi uptake (0.25 mM) was measured with increasing inhibitor concentrations (0.05-5 mM).
1008 Liposomes were preloaded with 30 mM Pi as the counter-exchange substrate. The data represent
1009 the arithmetic mean +/- SE of three independent experiments. ND, no competitive inhibitory
1010 constant could be measured under the given experimental conditions. DHAP, dihydroxyacetone
1011 phosphate; 3-PGA, 3-phosphoglycerate; PEP, phosphoenolpyruvate; Glc6P, glucose 6-P; Glc1P,
1012 glucose 1-P; Fru6P, fructose 6-P; Gal1P, galactose 1-P.

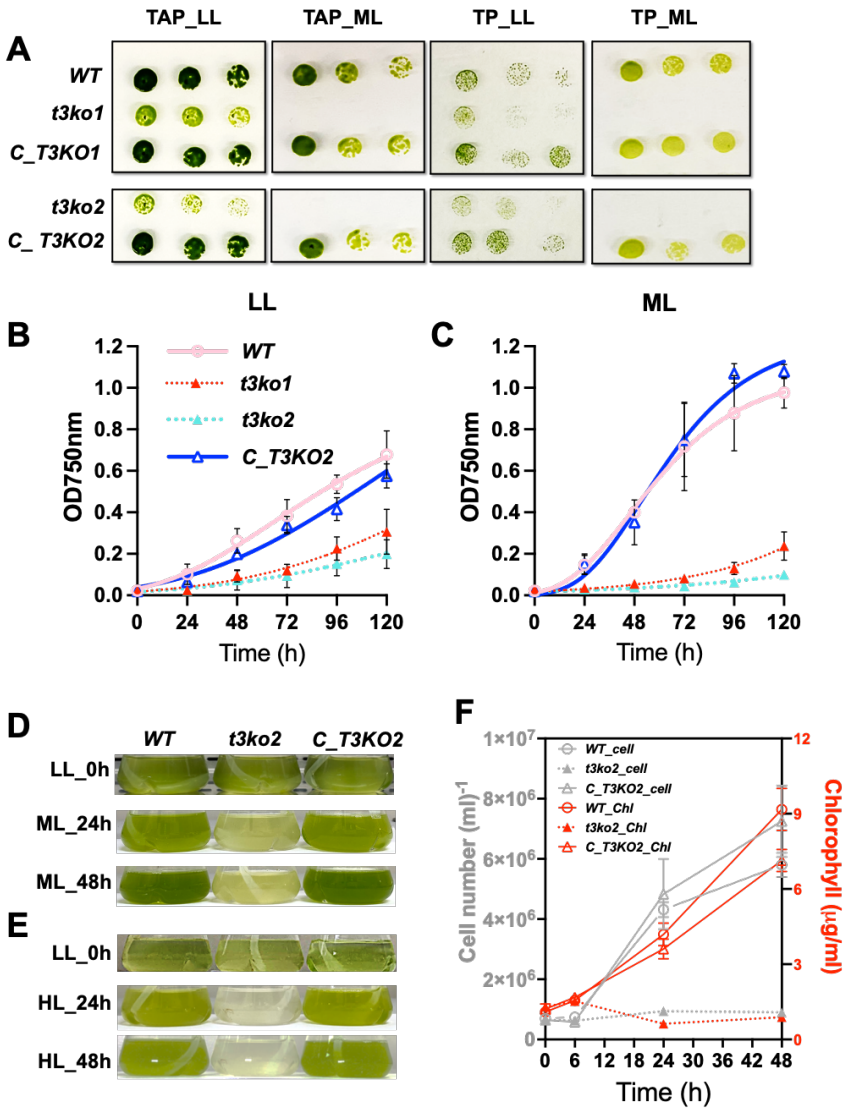

Fig. 2: Growth characterization of *tpt3* mutants and complemented strains. (**A**) Growth of WT, *t3ko1*, *t3ko2* and the complemented strains (*C_T3KO1* and *C_T3KO2*, respectively), at various dilutions (see below) on agar plates incubated under LL and ML for 4 d. Growth of respective strains in liquid medium under LL (**B**) and ML (**C**). The data represents the arithmetic mean (±SD) of three independent experiments. Transition of the strains from LL to ML (**D**) or to high light (HL, 450 µmol photons m^{-2} s^{-1}) (**E**) for the times indicated. (**F**) Cell growth (number) and chlorophyll content of the indicated cultures at various times following exposure to ML (from LL), for up to 48 h. In (**A**) the cells were spotted on agar plates containing TAP or TP medium under continuous LL or ML conditions. The dilution series used was 1.5, 0.75, 0.375 µg/mL chlorophyll (left to right). For growth in liquid medium, the cells were cultured in TP medium to an initial OD_{750nm} 0.02 in air and under continuous LL before initiating the various growth analyses in LL, ML or HL.

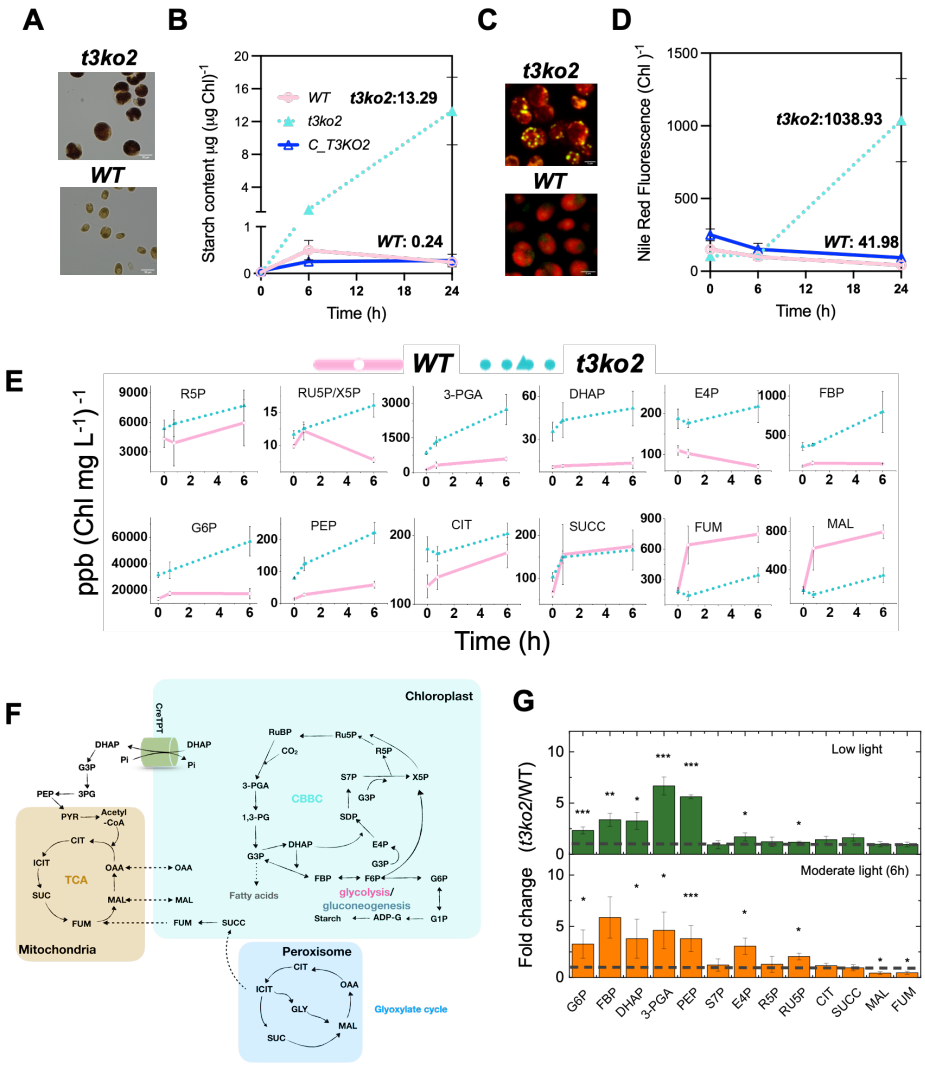

Fig. 3: Changes in storage carbon and metabolite levels in WT and *t3ko2* after transitioning the cells from growth in LL to ML. (A) Lugol staining of starch in WT and *t3ko2* after 48 h of ML. (**B**) Starch content in indicated strains following 0, 6, and 24 h of ML exposure. (**C**) Nile Red staining of TAG in WT and *t3ko2* following 48 h of ML exposure. (**D**) TAG content in the indicated strains following 0, 6, and 24 h of ML exposure. (**E**) Time course of metabolite accumulation at 0 h (LL), 45 min and 6 h following ML exposure. (**F**) Select metabolic pathways in Chlamydomonas adapted from Johnson and Alric, 2013(*79*). (**G**) Bar graph representation of fold-change for metabolites shown in (**E**), calculated by dividing the pool size in *t3ko2* by that of WT at the respective light levels. A fold change of 1 (no change) is shown by a dashed line. Each data point shows the mean and standard error; the data represents three biological replicates for each metabolite. An asterisk indicates statistically significant difference compared to WT (* P<0.05, ** P<0.01, *** P<0.001). Abbreviations: G6P, glucose-6-P; FBP, fructose bisphosphate; DHAP, dihydroxyacetone phosphate; 3-PGA, 3-phosphoglycerate; PEP, phosphoenolpyruvate; PYR, pyruvate; CIT, citrate; SUCC, succinate; FUM, fumarate; MAL, malate; E4P, Erythrose 4-P; R5P, Ribose 5-P; RU5P/X5P, ribulose 5-P/xylulose-5-P.

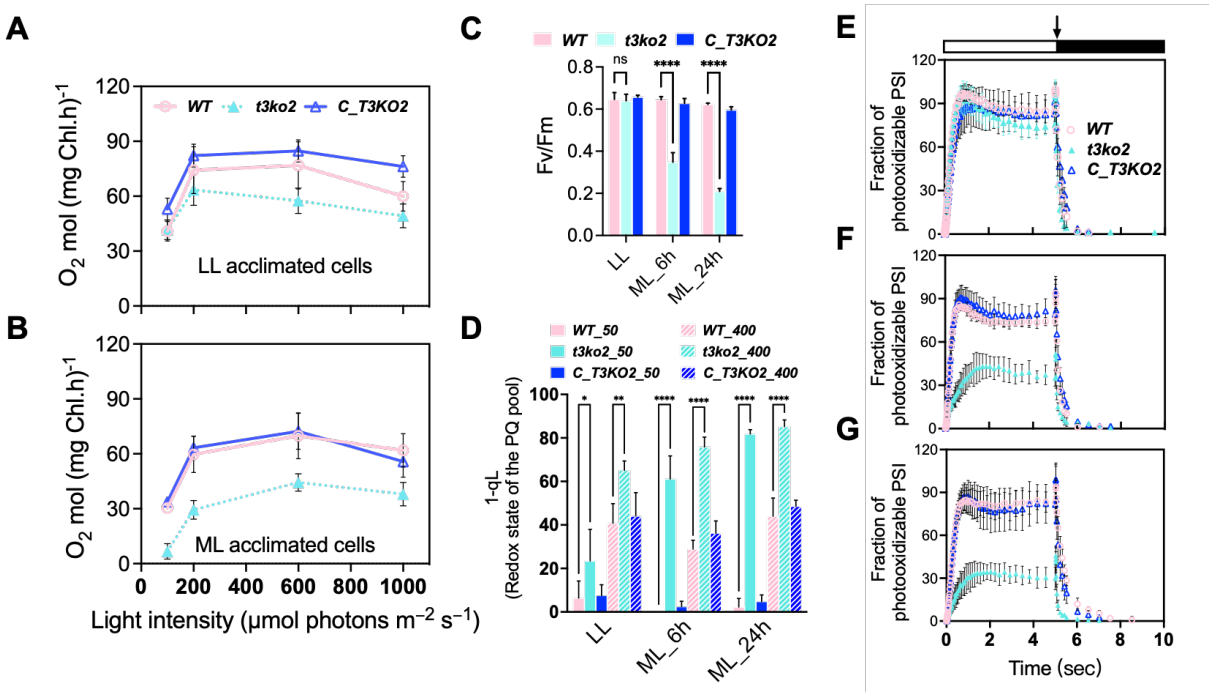

Fig. 4: Photosynthetic activities followed LL to ML transition. (**A**) O_2 evolution of LL-acclimated cells in the indicated strains. (**B**) O_2 evolution of ML-acclimated (24 h) cells. (**C**) Fv/Fm of WT, *t3ko2* and the rescued strain (*C_T3KO2*) following 6 and 24 h in ML. (**D**) 1-qL values (redox state of PQ pool) of LL- and ML-acclimated WT, *t3ko2* and the rescued strain. The acclimated cells were exposed to 50 and 400 µmol photons m^{-2} s^{-1}, as indicated, for 2 mins. (**E-G)** PSI activities following a LL to ML transition. P700 oxidation and reduction kinetics in LL-grown cells (**E**) and after 6 (**F**) and 24 h (**G**) in ML. Absorbance differences were monitored at 705 nm during continuous illumination with 150 µmol photons·m^{-2} s^{-1} for 5 sec (white box above), followed by a saturating light pulse at 1,500 µmol photons·m^{-2} s^{-1} (arrow) and a 5 sec dark incubation (black box). The data represent the arithmetic mean (±SD) of three independent experiments. Kinetics were normalized by setting maximum oxidation (after light pulse) for WT to 100%. For panels **c** and **d**, the asterisks represent significant differences determined by ANOVA tests. **P < 0.005, ****P < 0.0001.

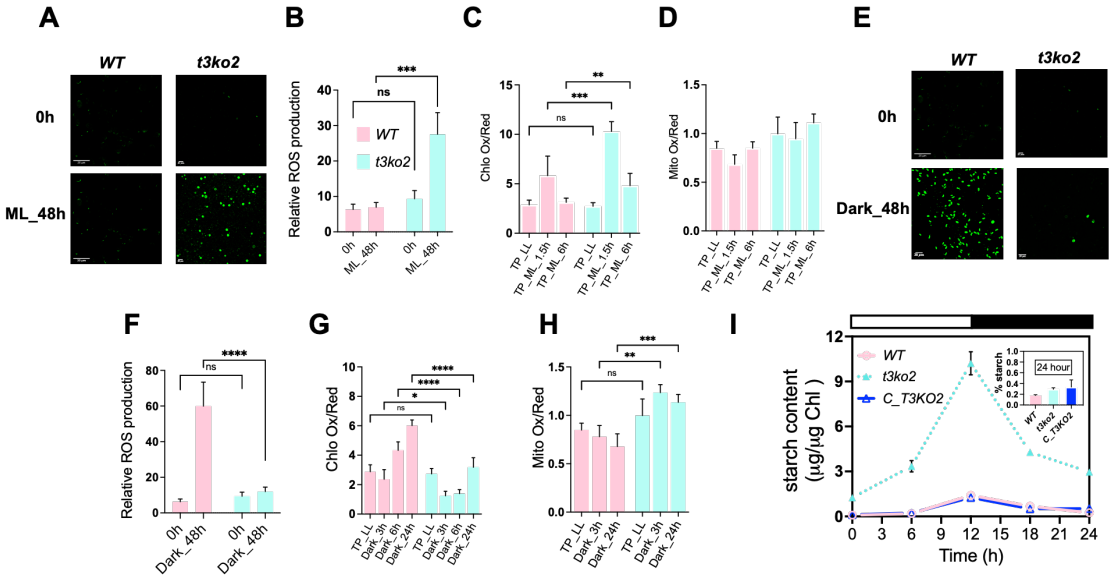

Fig. 5: Measurement of intracellular ROS. (**A**) ROS levels were evaluated by CM-H2DCFDA fluorescence of WT and the *t3ko2* mutant in LL and following exposure to ML for 48 h. (**B**) Quantitation of data in **a**. (**C-D**) Monitoring redox levels in chloroplasts (**C**) and mitochondria (**D**) after exposure of WT and the *t3ko2* mutant for 1.5 and 6.0 h of ML. **(E)** ROS levels monitored by CM-H2DCFDA staining in WT and *t3ko2* after the cells are transitioned from LL to darkness in TP medium. (**F**) Quantification of the data presented in **e**. Monitoring redox levels in chloroplasts (**G**) and mitochondria (**H**) in the dark with roGFP2 (targeted to chloroplast and mitochondria) in WT and the *t3ko2* mutant after various times in the dark. (**I**) Starch contents during diel cycle in indicated strains. The intensity of the light phase was 60 µmol photons m^{-2} s^{-1}. Values are means ± SD ($n \geq 3$). The asterisks represent a significant difference determined by an ANOVA test. **P < 0.005, ***P < 0.001. Strains were grown photoautotrophically under LL for 16-24 h. After dilution with fresh medium, cultures were transferred to ML or dark for the times indicated.

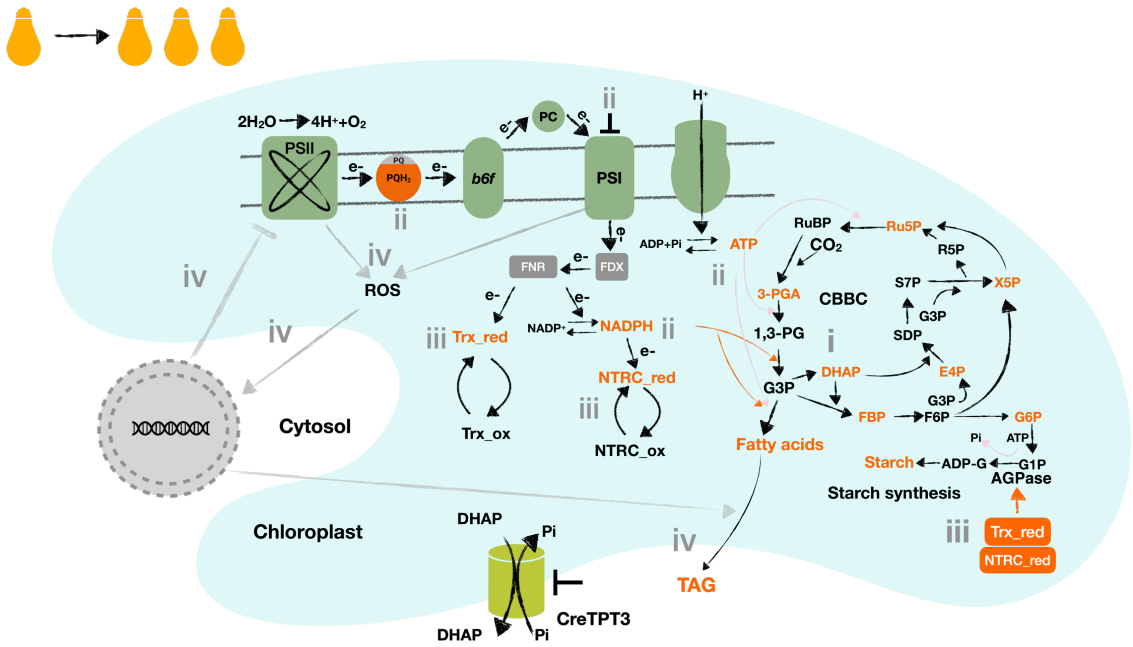

Fig. 6: Impact of eliminating Chlamydomonas TPT3 on the chloroplast metabolic landscape. **i.** reduced triose-P export leads to accumulation of the sugar-P in CBBC and glycolysis pathways (e.g. triose-P, hexose-P, marked in orange), and an elevated ratio of 3-PGA/Pi (which can allosterically activate AGPase activity) would begin to stimulate production of storage carbon; **ii.** CBBC activity diminishes as a consequence of the hyper-accumulation of the precursors along with the fixation of CO_2, leading to elevation of reductant (NADPH) and energy (ATP) within the chloroplast; the elevated NADPH:$NADP^+$ and ATP:ADP ratios, elicit strong feedback on PET causing hyper-reduction of electron carriers (eg: over reduced PQ pool and highly reduced PSI) that slows electron flow across the cytochrome b_6f complex; **iii.** the highly reduced PET system and the elevated NADPH can actively reduce FDX/TRX and the NTRC, respectively; reduced TRX and/or NTRC can activate the AGPase (above the activity elicited by an increase in the 3-PGA/Pi ratio), leading to additional starch accumulation; **iv.** hyper-reduction of PET can also lead to ROS accumulation, that can act as a signal controlling expression of chloroplast and nuclear genes; ROS also cause damage to both PSII and I and lead to neutral lipid (TAG: triacylglycerol) accumulation as a consequence of activation of diacylglycerol acyltransferases (DGAT) and phospholipid diacylglycerol acyltransferase (PDAT). Many of these metabolic/acclimatory processes both overlap and are interconnected. Under conditions of extended exposure to moderate light, the damage in the Chlamydomonas *tpt3* mutant can accumulate and lead to cell death; cell death occurs rapidly in high light.

1099 **Supplementary Materials**
1100

1101 **Materials and methods**

1102 **Extraction of samples for LC-MS/MS**

1103 To each cell pellet, 500 µL methanol was added along with the internal standards ribitol and PIPES
1104 to a final concentration of 2 µM each. Samples were then vortexed for 30 sec, frozen in liquid
1105 nitrogen as described in(*80*), and allowed to thaw at 0°C. This vortex-freeze-thaw cycle was
1106 repeated twice more before the samples were centrifuged at 10,000 x g at 1°C for 5 min. The
1107 supernatant was collected, and the remaining pellets were extracted twice more with 500 µL of a
1108 50:50 mixture of methanol and water, with 3 vortex-freeze-thaw cycles done for each extraction.
1109 Supernatants from each extraction procedure were pooled and dried on a Thermo Fisher SpeedVac
1110 Concentrator. Dried extracts were then resuspended in 500 µL water and cleaned to remove any
1111 residual large cell debris by filtration, first through a 0.22 µm pore size Spin-X centrifugal tube
1112 filter, followed by 10 K molecular mass cutoff filters, followed finally by 3 K molecular mass
1113 cutoff filters. After each filtration step, filters were rinsed with 50 µL water, which was added to
1114 the total sample volume for subsequent steps. Filtered extracts were dried again and resuspended
1115 in 200 µL water for LC-MS/MS analysis.

1116 **Analysis of metabolite extracts**

1117 Metabolite extracts were analyzed using an LC-MS/MS method adapted from(*78*). A Phenomenex
1118 150 mm x 2 mm Synergi Hydro-RP column was used on an Agilent 1200 Series HPLC system
1119 coupled to an AB Sciex 5500 QTRAP system. LC was performed with a liquid injection volume
1120 of 20 µL, using gradient elution of 10 mM tributylamine and 15 mM acetic acid (aqueous phase)
1121 and acetonitrile (organic phase) at a constant flow rate of 0.3 mL/min, and a constant temperature
1122 of 40°C. The gradient profile of the organic phase is as follows: 0% B (0 min), 8% B (10 min),
1123 16% B (15 min), 30%B (16.5 min), 30% B (19 min), 90% B (21.5 min), 90% B (28 min), 0% B
1124 (28.5 min), and 0% B (35 min). MS analysis was performed in negative mode using a multiple
1125 reaction monitoring (MRM) acquisition method. Data acquisition was performed on the ABSciex
1126 Analyst 1.7 software. Absolute quantification of intracellular metabolites was performed using the
1127 quantitation mode on the Analyst software.

1128 **Protein extraction and immunoblot analysis**

1129 Affinity-purified polyclonal antibodies to CreTPT3 were custom-made by GenScript. The antigen
1130 sequence used for antibody generation was KSWSFGRPVTKQEF. Chlamydomonas cells were
1131 grown in liquid cultures to 2–5 x10^6 cells ml^{-1} and collected by centrifugation (2700 rpm, 5 min).
1132 Cells were resuspended in resuspension buffer [(5 mM HEPES, pH 7.5, KOH), 10 mM EDTA (pH
1133 7.5, NaOH), 1x protease inhibitor "complete EDTA-free" (Roche)]. For the disruption of cells,
1134 bead-beating was performed using a mini beadbeater (Biospec) in two cycles of 30 sec min^{-1}, with
1135 a 1 min period of cooling on ice between cycles. Disrupted cells were centrifuged at 4°C, 30 min,
1136 14000 rpm in a microfuge. The supernatant was removed, the pellet was resuspended in sample
1137 buffer (resuspension buffer supplemented with 100 mM Na_2CO_3, 100 mM DTT, 2% WT/vol SDS,
1138 and 12% WT /vol sucrose).

1139 SDS-PAGE was performed using a 12% polyacrylamide gel (Bio-Rad), with the electrophoresis
1140 for 90 min at 120 V. Next, proteins were transferred onto a PVDF membrane (Bio-Rad) using
1141 Trans-Blot Turbo (Bio-Rad). The detection was performed using Clarity Max Western ECL
1142 Substrate (Bio-Rad).

1143 **RT-qPCR**

1144 RT-qPCR, was performed as described previously(*69*). Briefly, total RNA was isolated using the
1145 RNeasy Plant Mini Kit (Qiagen) and treated with DNase I (Qiagen). First-strand cDNA was
1146 generated by reverse transcription of 0.5 µg total RNA using the iScript cDNA Synthesis Kit (Bio-
1147 Rad). Real-time PCR using the Roche Light Cycler 480 was performed with the SensiMix NO-
1148 Rox SYBR Green I Kit as described by the manufacturer (Bioline). Oligos used in this research
1149 for analyzing the expression levels of Cre*TPT1/2/3/25* are listed in **Supplemental Table 1**.

1150 **Analysis of transcript levels in response to different conditions**

1151 In order to analyze the transcript level of Cre*TPT* genes under different conditions, we obtained
1152 RNAseq data published previously in which cells experienced a diurnal cycle, nitrogen starvation,
1153 sulfur starvation and Fe^{2+} starvation(*81–85*). The log2 fold change of each gene was calculated
1154 based on the ratio of transcript abundance at different time point over transcript level at time point
1155 0 h. The fold change was visualized by a heatmap and the color bar is the scale of log2 (fold-
1156 change).

1157 **In vivo polymeric carbohydrate staining**

1158 Lugol's iodine (aqueous solution of 1.8% iodine and 3.0% potassium iodide) was used to stain in
1159 vivo polymeric carbohydrate. Briefly, 0.5 mL of the cell culture was pelleted, resuspended in 10
1160 µL of Lugol's iodine and visualized under a bright-field microscope. Lugol's iodine selectively
1161 binds to alpha-1,4 glucans and stains it blue-black.

1162

1163

1164

oligo name	sequence
gTPT3_pRam118_f	tactcacaacaagcccagttATGGCTTCGCTCGCTCAGCGCGTGAGC
gTPT3_pRam118_r	agcggggatccttatccgttTTAGGCCGCGGCCGGCGACGC
TPT3pro1000_f	gccttttgctcacatgtggcggccgccgccatgctggccaacag
TPT3pro1000_r	taccaatccacaaatgtgggctagcccatgtgaaggcgttgacc
TPT3_3UTR_f	gatgacgacaagtaaagatctTAAGGCGGGCAGCGGC
TPT3_3UTR_r	GCGCAAGAAAGAAGCTTGATATCCCCCTTATAATGTTTACAAGTGGTGCG
hygro_crispr_f2	GGAACTGGCGCAGTTCCTCTG
hygro_crispr_re2	GGCTCGCGTAGGAATCATCCG
TPT3_gRNA1_F	GCTCGGTTGAGCGCACCC
TPT3_gRNA1_R	CAAGGGTCTGGCGAGCACG
TPT3_gRNA2_F	ACCTCCCCATCGCCACGAT
TPT3_gRNA2_R	AGGGGTAAGGACAGCGGTG
Qrt_TPT1_f2	CCTGTACCAGCAGGTGTCGTAC
Qrt_TPT1_r2	CCAGCGCGTTCTGGAGTGACA
Qrt_TPT2_f2	ATGGCGTCTCTGCTGGGC
Qrt_TPT2_r2	CTGCTCGCCCATTCTCCTC
Qrt_TPT3_f2	GCAAAGCTGGCGCCTACTG
Qrt_TPT3_r2	TAGACCAGGCCGACCACCAC
Qrt_TPT25_f1	CTGGTTCATCGGGACATGGC
Qrt_TPT25_r1	TGGCTGAAGCTGACCACT

Supplementary Table 1: Oligonucleotide list.

Cre ID	Name	Prediction	CS Position
Cre08.g379350.t1.1	CreTPT1	cTP	CS pos: 61-62. TCL-AV.
Cre06.g263850.t1.1	CreTPT2	cTP	CS pos: 70-71. VCQ-AA.
Cre01.g045550.t1.2	CreTPT3	cTP	CS pos: 60-61. VTK-AS.
Cre02.g106200.t1.2	CreTPT4	OTHER	
Cre02.g112900.t1.2	CreTPT5	OTHER	
Cre02.g144300.t1.2	CreTPT6	OTHER	
Cre03.g162000.t1.2	CreTPT7	OTHER	
Cre03.g184850.t1.1	CreTPT8	OTHER	
Cre04.g227450.t1.2	CreTPT9	OTHER	
Cre07.g330850.t1.1	CreTPT10	OTHER	
Cre08.g363600.t1.2	CreTPT11	OTHER	
Cre09.g408400.t1.1	CreTPT12	OTHER	
Cre09.g413700.t1.1	CreTPT13	OTHER	
Cre08.g382350.t1.2	CreTPT14	OTHER	
Cre09.g415900.t1.2	CreTPT15	OTHER	
Cre10.g452750.t1.2	CreTPT16	OTHER	
Cre11.g479950.t1.2	CreTPT17	OTHER	
Cre12.g490050.t1.2	CreTPT18	OTHER	
Cre12.g490100.t1.2	CreTPT19	OTHER	
Cre12.g501000.t1.1	CreTPT20	OTHER	
Cre15.g641266.t1.1	CreTPT22	OTHER	
Cre15.g642950.t1.2	CreTPT23	OTHER	
Cre15.g643385.t1.1	CreTPT24	OTHER	
Cre16.g663800.t1.2	CreTPT25	cTP	CS pos: 70-71. IVA-SS.
Cre16.g666250.t1.2	CreTPT26	OTHER	
Cre17.g702700.t1.1	CreTPT27	OTHER	
Cre17.g703250.t1.2	CreTPT28	OTHER	
Cre17.g710850.t1.2	CreTPT29	OTHER	
Cre11.g467754.t1.1	CreTPT30	OTHER	
Cre14.g622700.t1.2	CreTPT31	OTHER	
Cre18.g748947.t1.1	CreTPT32	OTHER	
Cre09.g408428.t1.2	CreTPT33	OTHER	

Supplementary Table 2: Members of the triose phosphate transporter family in *Chlamydomonas reinhardtii* and their predicted subcellular localization based on TargetP-2.0. cTP, chloroplast transit peptide; CS position, transit peptides cleavage site.

Name	D_11h	D_9h	D_7h	D_5h	D_3h	D_1h	D_0.5h	D_0h	L_0.5h	L_1h	L_3h	L_5h	L_7h	L_9h	L_11h	D_13h
TPT1	5.2883	10.2702	9.45732	8.85549	7.70518	6.18466	7.5509	9.07019	0.511726	0.198621	0.329098	1.99425	2.93498	2.13736	1.02291	9.56813
TPT2	6.46543	9.45107	9.77461	10.5338	12.8513	8.72194	9.51834	10.275	59.1606	62.7836	33.5533	12.891	5.69013	5.94982	12.1866	3.6131
TPT3	233.805	337.793	247.287	181.496	131.602	97.1854	105.57	98.3637	71.9013	43.1935	218.026	280.947	185.973	179.459	157.828	312.135
TPT25	38.9867	62.7835	45.3561	32.7872	22.8554	14.8691	15.5851	13.8916	19.6257	26.8661	10.2213	7.48595	8.11458	19.7874	32.0979	53.4145

Supplemental Table 3: Expression levels of TPTs over the diel cycle in Chlamydomonas. Data were extracted from(*81*).

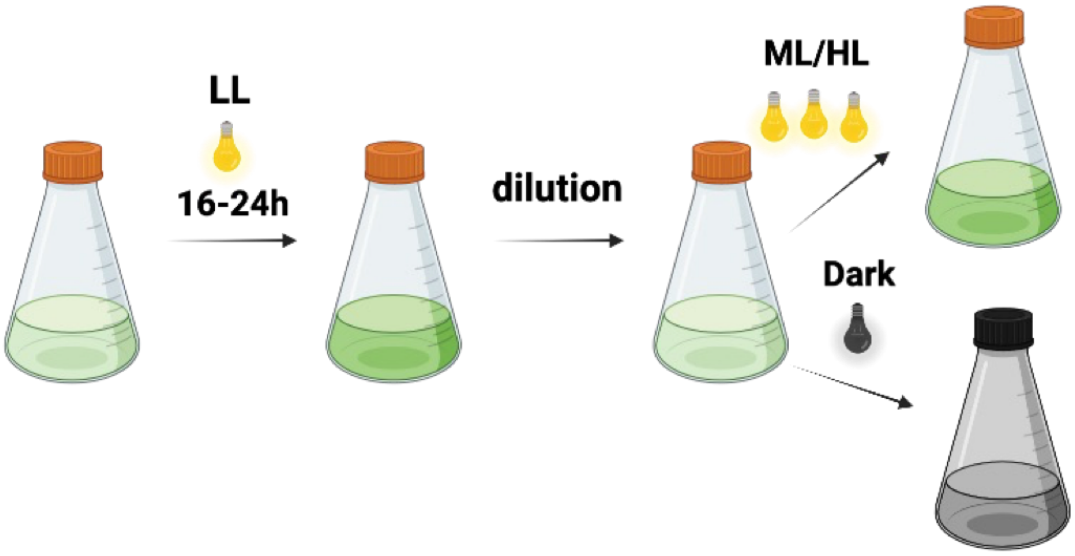

1175
1176 **Supplementary Fig. 1: Experimental set up.** All strains were grown photoautotrophically under
1177 low white light (LL, ~30 µmol photons m^{-2} s^{-1}) for 16-24 h. After dilution with fresh medium, the
1178 cultures were transferred to moderate light (ML, 250-300 µmol photon m^{-2} s^{-1}). On occasion, the
1179 cultures were also transferred to the dark or high light (~450 µmol photon $m^{-2}s^{-1}$) for 24 or 48 h.
1180 To avoid self-shading, the culture density was adjusted to 1-1.5 µg/mL chlorophyll before
1181 exposure to ML or HL.

1182

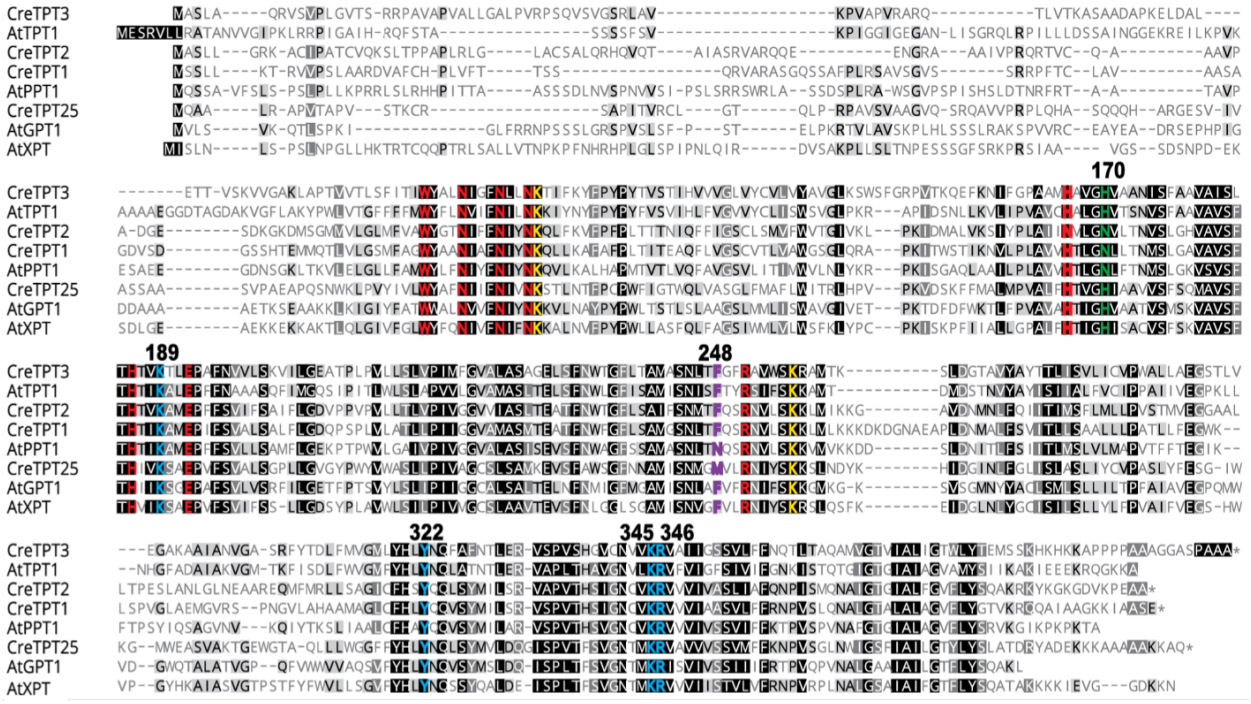

Supplementary Fig. 2: Sequence alignment of the plastid phosphate transporter sequences of *Arabidopsis thaliana* and *Chlamydomonas reinhardtii.* Plastid TPTs from Chlamydomonas are CreTPT1 (Cre08.g379350.t1.1), CreTPT2 (Cre06.g263850.t1.1), CreTPT3 (Cre01.g045550.t1.2), and CreTPT25 (Cre16.g663800.t1.2). Sequences from *Arabidopsis thaliana* are AtTPT1 (AT5G46110.1), AtPPT1 (AT5G33320.1), AtGPT1 (AT5G54800.1) and AtXPT1 (AT5G17630.1). Conserved substrate binding pockets are colored red. Phosphate-binding residues are highlighted with blue. The gate capping residues are marked with yellow. The positions of residue in green are crucial for the preference of triose-phosphate or 3-PGA as substrate. The positions of purple residues are critical for the specificity of PEP.

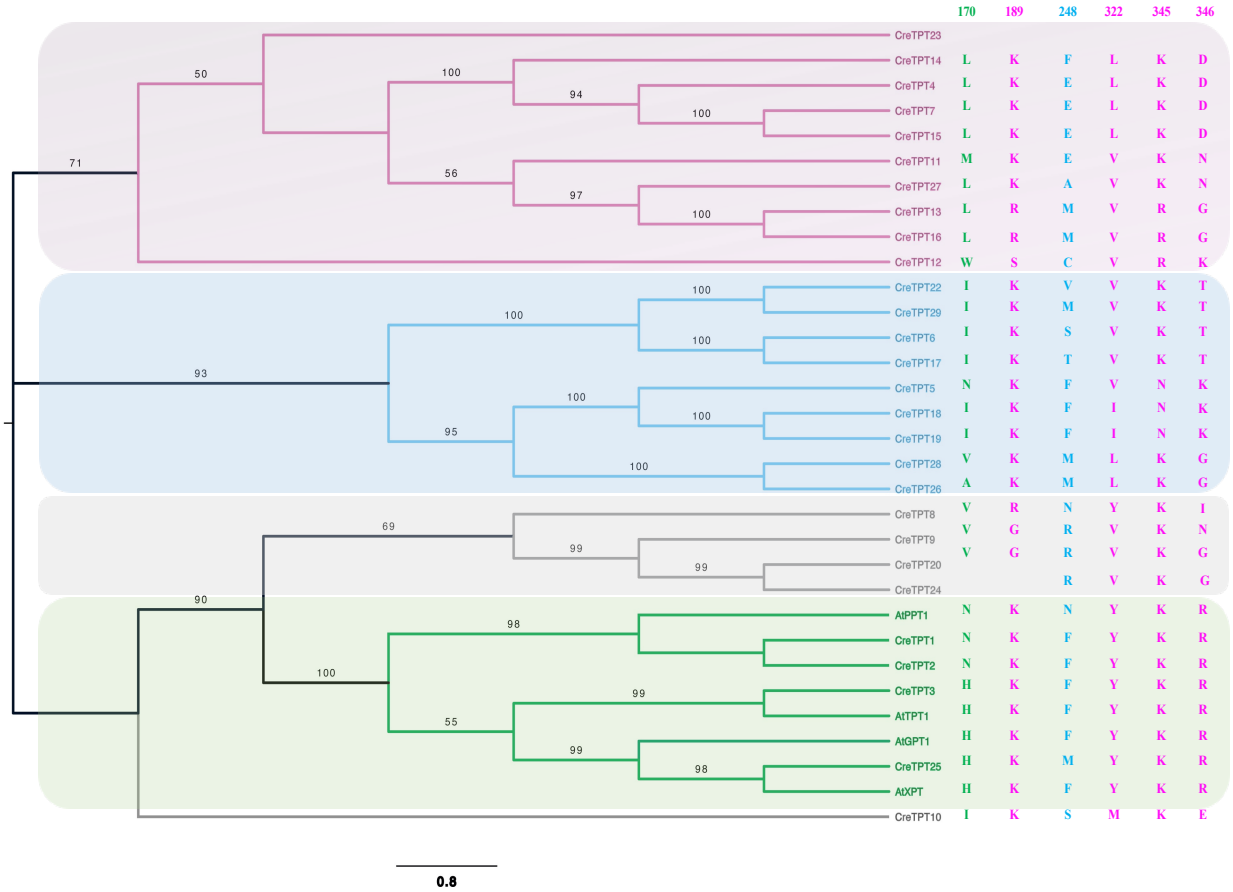

Supplementary Fig. 3: Phylogeny of TPT homologues in Chlamydomonas. Amino acid residues at the positions responsible for substrate specificity in TPT homologues are listed. The numbers above the amino acids are the position of each residue in CreTPT3. The residues marked with green, blue and purple colors are crucial for the preference of triose-phosphate or 3-PGA, for the specificity of PEP and for the binding of phosphate, respectively. Plastid PPT, XPT, and TPT from *Arabidopsis thaliana* are included in the analysis.

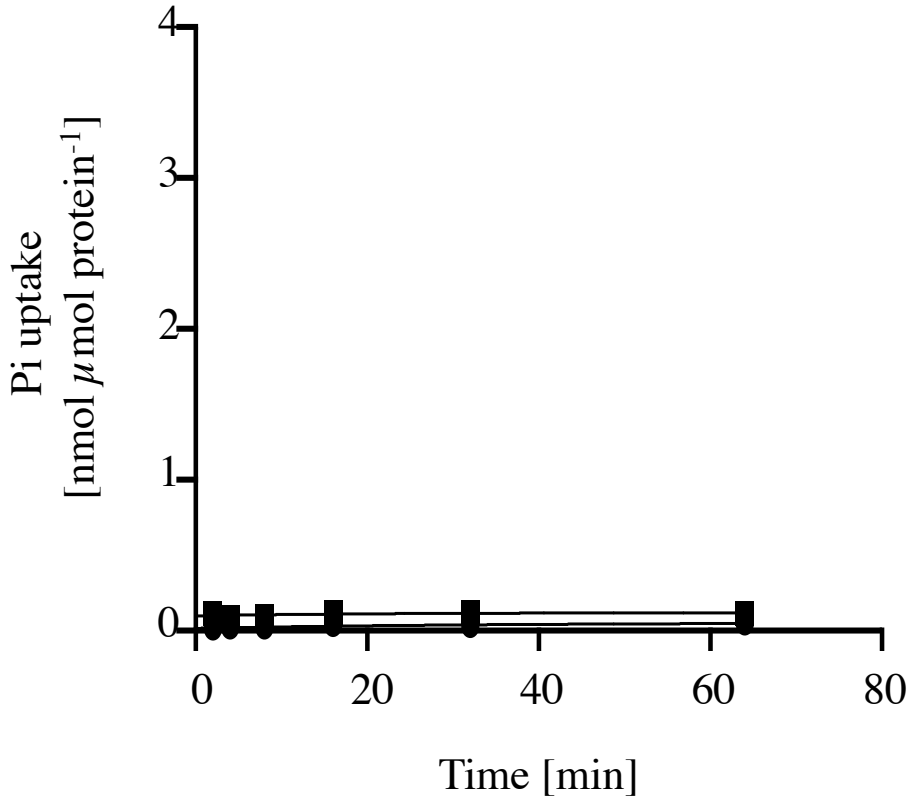

1202

1203 **Supplementary Fig. 4: Background activity of Pi uptake derived from the endogenous yeast**
1204 **transporter reconstituted into liposomes.** Time-dependent uptake of Pi (0.25 mM) into
1205 reconstituted liposomes preloaded with 30 mM of Pi (■) or without exchange substrate (●)
1206 prepared from yeast cells harboring the empty vector (pYES-NTa). The arithmetic mean (±SD) of
1207 three independent experiments (each with three technical replicates) was plotted against time. The
1208 observed Pi uptake rates of endogenous yeast carrier reconstituted into liposomes were negligible
1209 compared to the rates of His-CreTPT3 (20-fold higher, **Fig. 1D**), indicating that this expression
1210 system is suitable for functional analysis of recombinant phosphate transporters.

1211

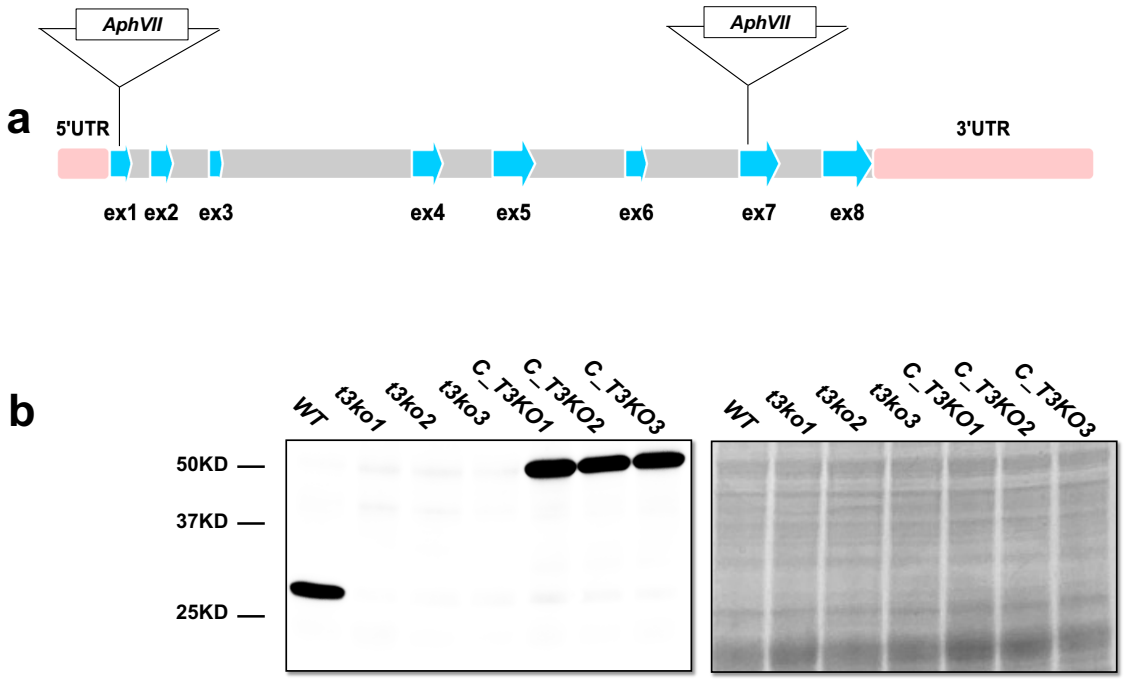

1212

1213 **Supplementary Fig. 5: Inactivation of Cre*TPT3* by CRISPR-Cas9.** (**A**) Molecular map of
1214 Cre*TPT3* gene and positions of the Cas9 targeted sites. The edited sites are located in exons 1 and
1215 7; *t3ko1* has the marker gene inserted in exon 1 and *t3ko2* and *t3ko3* has the marker gene inserted
1216 in exon 7. (**B**) Immunoblot (left panel) and loading control (right panel) of wild type, *t3ko1*, *t3ko2*,
1217 *t3ko3* and the complemented strains (*C_T3KO1*, *C_T3KO2* and *C_T3KO3*, respectively).

1218

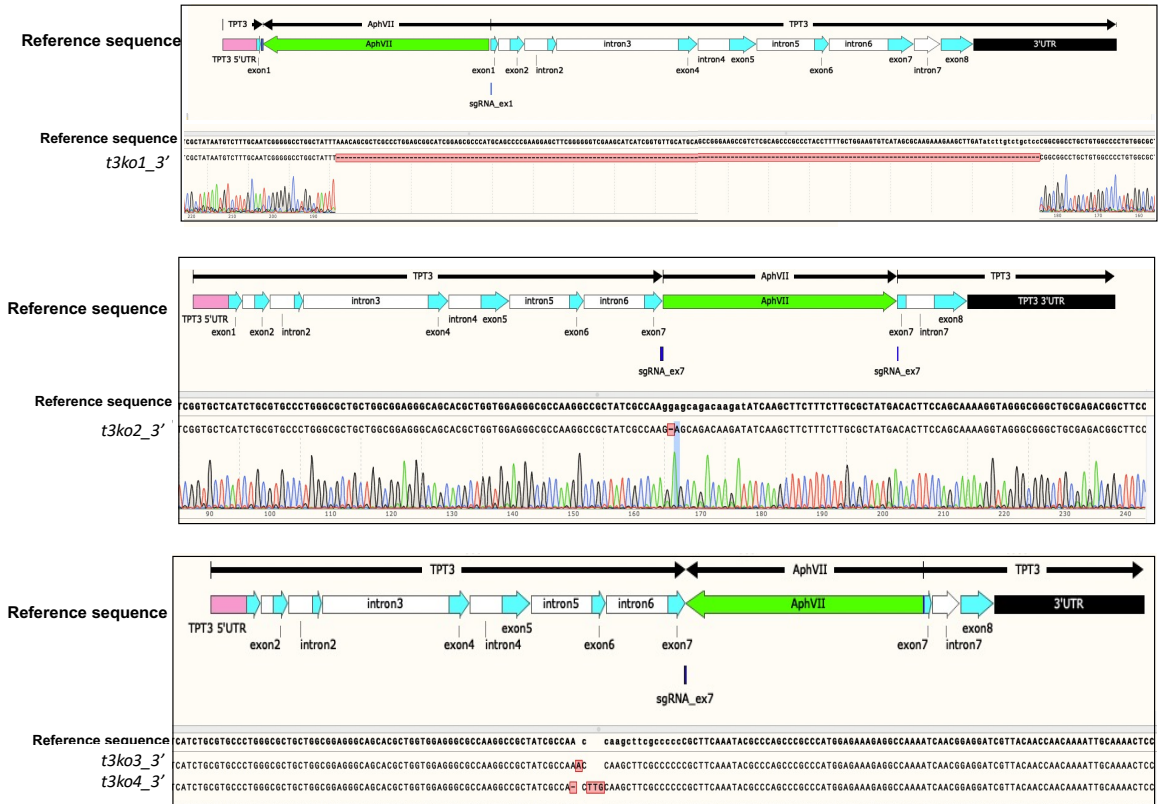

Supplementary Fig. 6: Sequencing of genomic DNA fragments across the site of insertion of the drug resistant marker (*AphVII* cassette, which confers hygromycin resistance) in the different *tpt3* mutants (*t3ko1*, *t3ko2*, *t3ko3* and *t3ko4*).

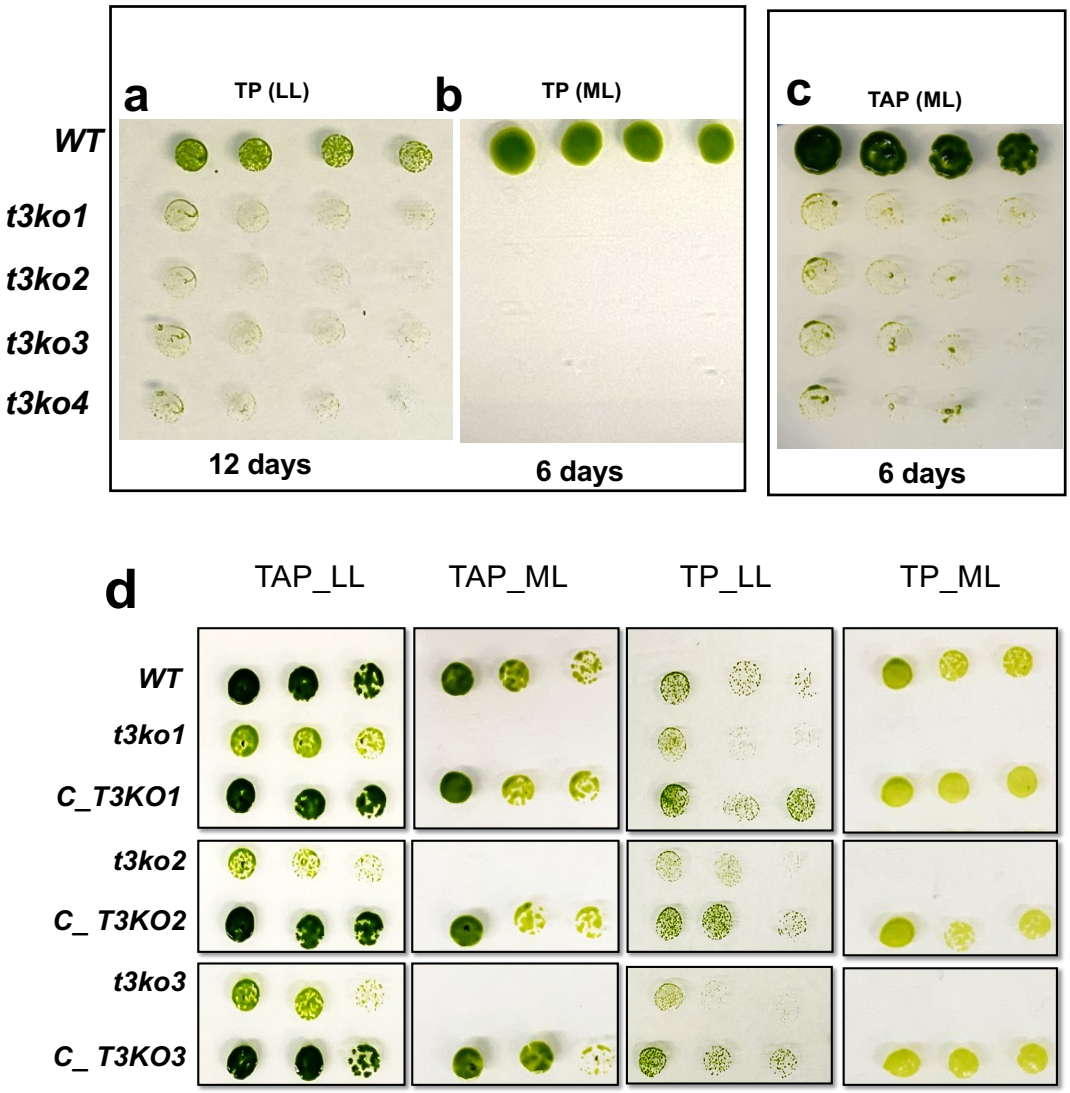

Supplementary Fig. 7: Growth of the CRISPR-Cas9 generated Cre*tpt3* mutants on solid medium. (**A**) The various mutant strains (*t3ko1*, *t3ko2*, *t3ko3*, *t3ko4*) and WT were spotted on plates containing TP medium under continuous LL or (**B**) ML. (**C**) Cells were spotted on agar plates containing TAP medium under continuous ML. The dilution series from (**A**,**B**,**C**) were 2.0, 0.75, 0.375 µg/mL chlorophyll. (**D**) Growth of wild type (WT), *t3ko1*, *t3ko2*, *t3ko3* and the complemented strains on agar plates containing TAP or TP medium under LL or ML for 4 d. The dilution series used was 1.5, 0.75, 0.375 µg/mL chlorophyll.

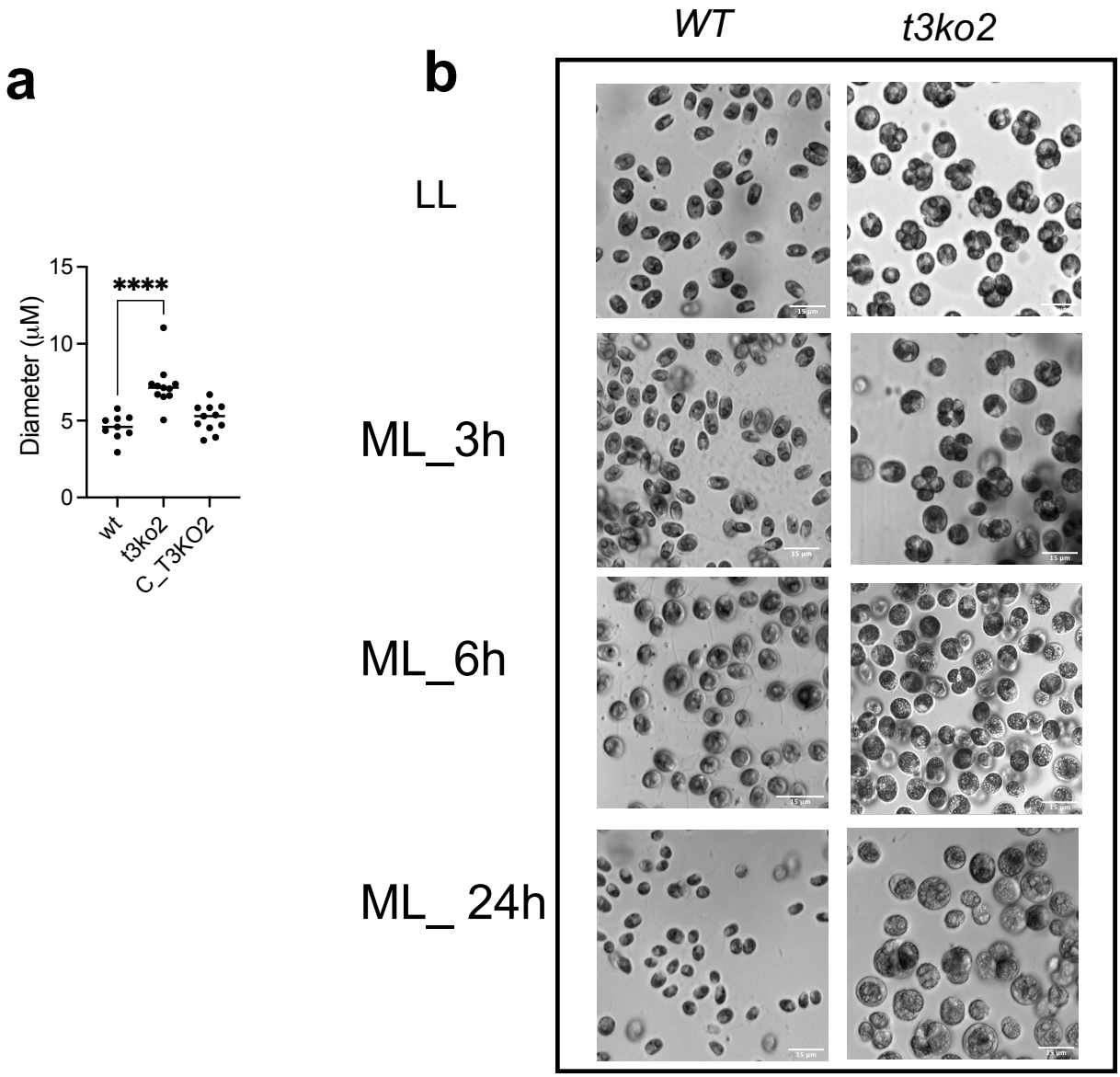

1234

1235 **Supplementary Fig. 8: (A)** Cell size of WT, *t3ko2*, and *C_T3KO2* in TP under both LL and ML.
1236 **(B)** WT and *t3ko2* morphology following a LL to ML transition.

1237

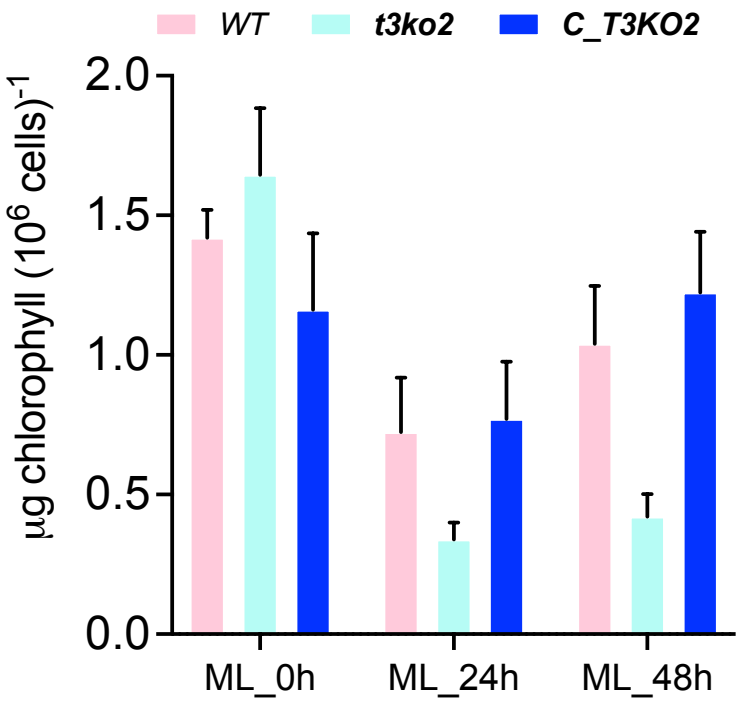

1238

1239 **Supplementary Fig. 9: Quantification of chlorophyll contents in indicated strains after**
1240 **exposure to ML for 24 and 48 h.** All strains were grown photoautotrophically under LL for 16-
1241 24 h. After dilution with fresh medium, the culture was transferred to ML for over 24 h. The initial
1242 inoculum density used for the transition was between 1-1.5 µg/mL chlorophyll in order to avoid
1243 self-shading.

1244

1245

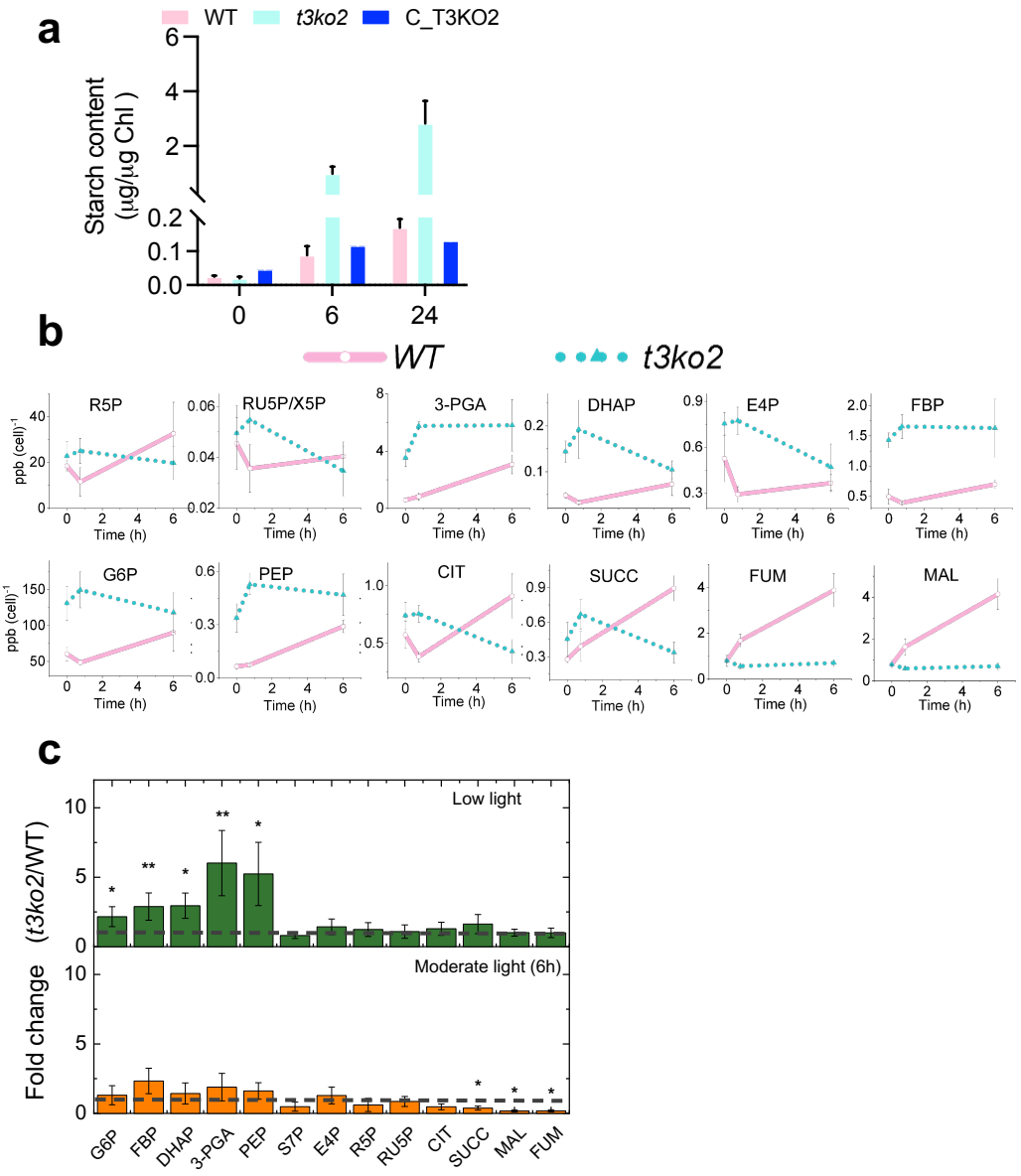

Supplementary Fig. 10: Starch and metabolites in WT and *t3ko2*. (**A**) Starch contents in indicated strains following 0, 6, and 24 h of LL exposure in TP. (**B**) Time course of change in the metabolite pool sizes at 0 h (LL), 45 min and 6 h after shifting LL-grown cells to ML. Data was normalized to cell numbers. (**C**) Schematic representation of the fold-change for the metabolites shown in (**B**), calculated by dividing the pool size in *t3ko2* by that of WT cells under the same conditions. Fold change of 1 (no change) is shown by a dashed line. Each data point is the mean and standard error of three biological replicates. Asterisk indicates statistically significant differences relative to WT (* P<0.05, ** P<0.01, *** P<0.001). Abbreviations: G6P, glucose-6-phosphate; FBP, fructose bisphosphate; DHAP, dihydroxyacetone phosphate; 3-PGA, 3-phosphoglycerate; PEP, phosphoenolpyruvate; CIT, citrate; SUCC, succinate; FUM, fumarate; MAL, malate; S7P, sedoheptulose-7-phosphate; E4P, Erythrose 4-phosphate; R5P, Ribose 5-phosphate; RU5P/X5P, ribulose 5-phosphate/xylulose-5-phosphate;

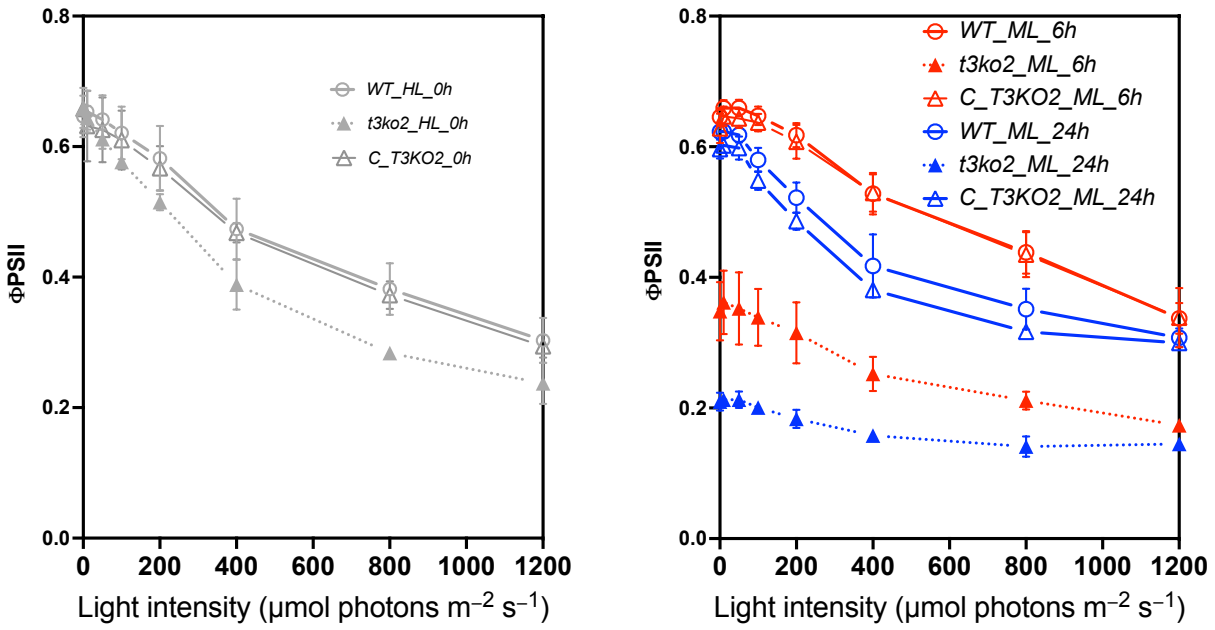

Supplementary Fig. 11: Quantum yield of PSII (ΦPSII) grown in LL (0 h: left panel) and after 6 and 24 h of growth in ML (right panel) following exposure to increasing actinic light intensities.

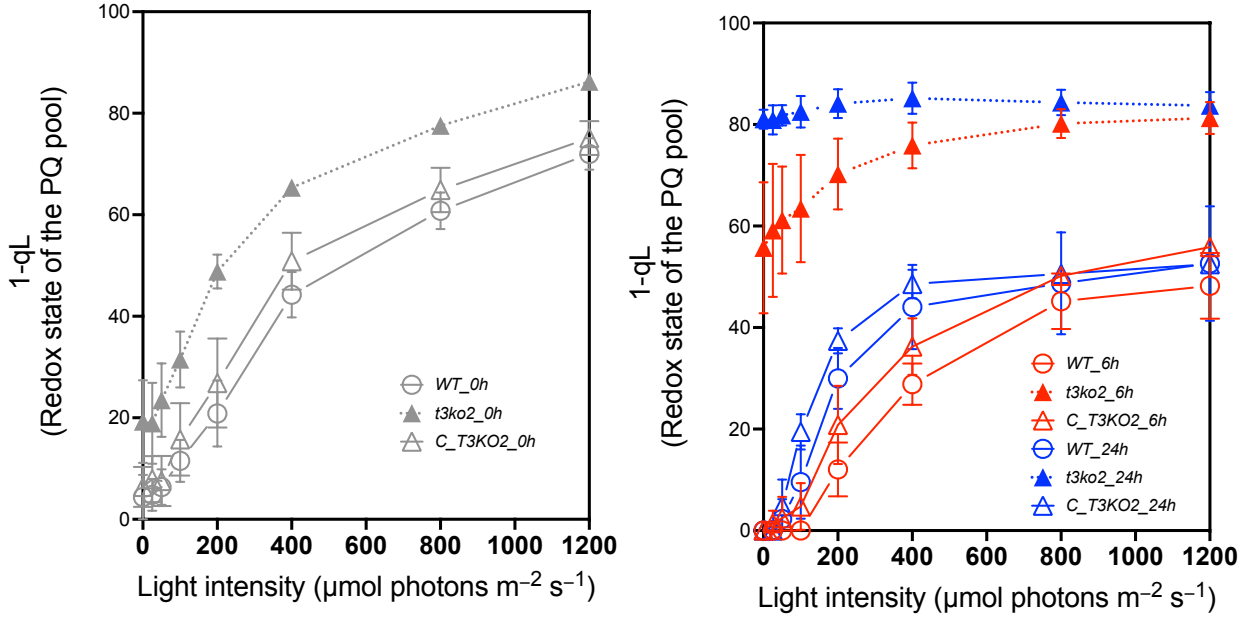

Supplementary Fig. 12: Redox state of the PQ pool following a LL to ML transition at different actinic light intensities. 1-qL values of LL (left panel) and ML (right panel) acclimated cells exposed to increasing light intensities.

1268

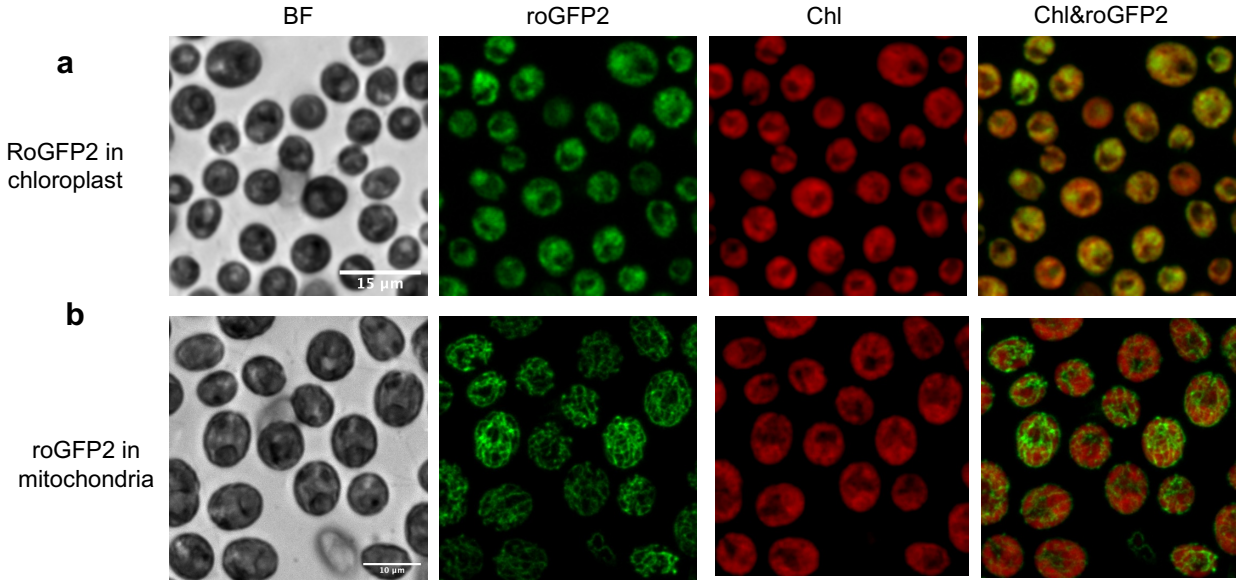

1269

1270 **Supplementary Fig. 13:** Redox-sensitive GFP (roGFP) protein was targeted to the chloroplast (**A**)
1271 and mitochondrion (**B**). BF: bright field; roGFP2 fluorescence: green; Chlorophyll (Chl)
1272 autofluorescence: red.

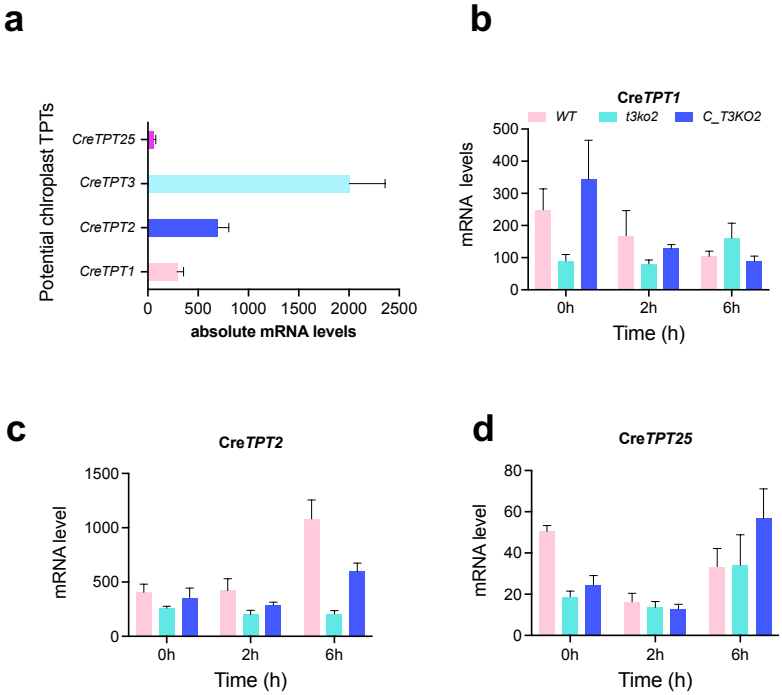

1273

1274 **Supplementary Fig. 14:** (**A**) mRNA levels of the putative chloroplast envelope localized TPTs
1275 under LL during growth in TP medium. mRNA levels of CreTPT1 (**B**), CreTPT2 (**C**) and
1276 CreTPT25 (**D**) in the indicated strains 0, 2, 4 h after the cells were shifted from LL to ML.

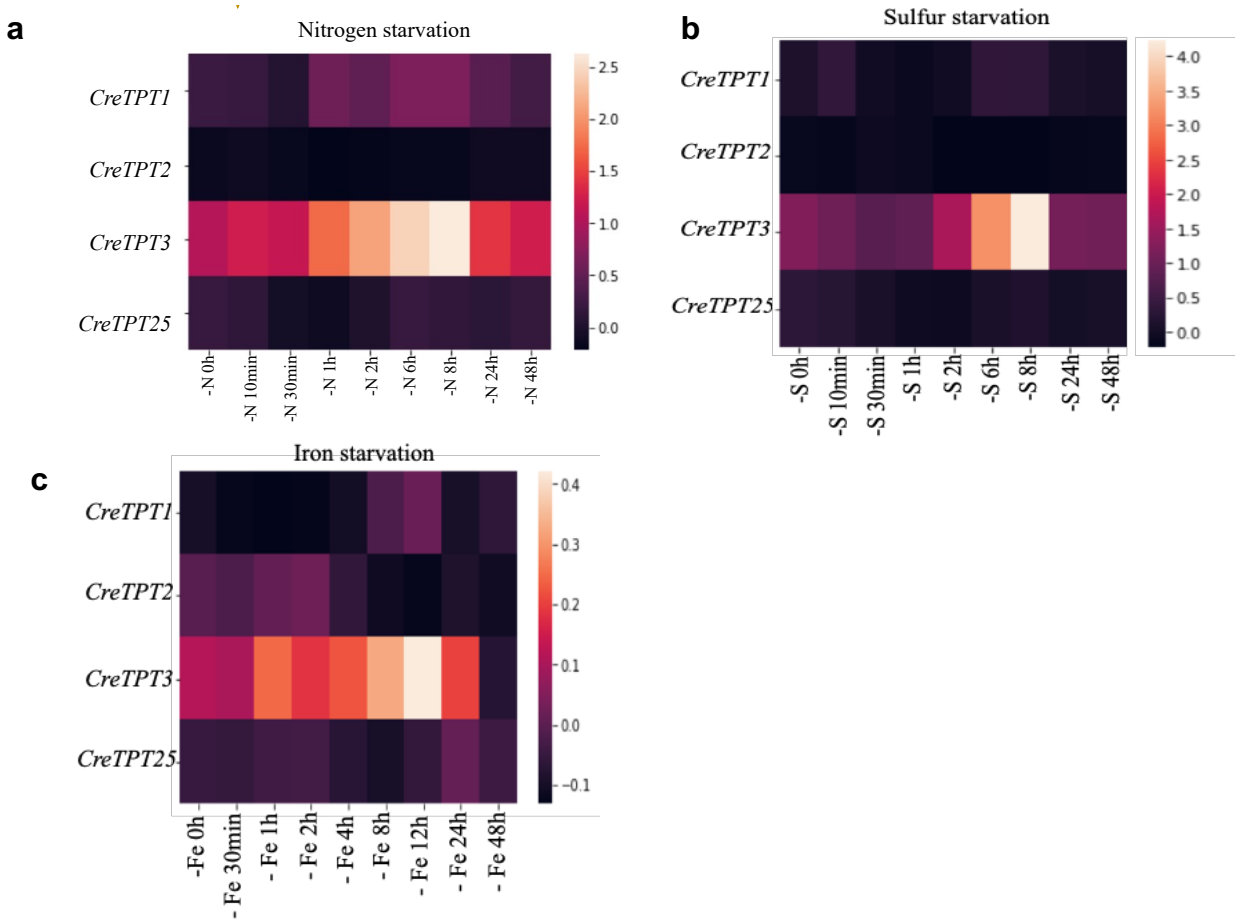

Supplementary Fig. 15: Expression of the putative chloroplast envelope localized TPTs under nitrogen starvation **(A)**, sulfur starvation **(B)**, and **(C)** iron starvation(*83–85*).